An efficient temperature-dependent crystal plasticity framework for pure magnesium with emphasis on the competition between slip and twinning

Journal Article

Author(s):
Hollenweger, Yannick; Kochmann, Dennis M. (ID)

An efficient temperature-dependent crystal plasticity framework for pure magnesium with emphasis on the competition between slip and twinning

Yannick Hollenweger, Dennis M. Kochmann [*]

Mechanics & Materials Lab, Department of Mechanical and Process Engineering, ETH Zürich, 8092 Zürich, Switzerland

ARTICLE INFO

ABSTRACT

Experimental evidence suggests that the formation of compressive twin bands and the associated strain localization is a key driver behind the low ductility of magnesium (Mg) at ambient temperature, which is why processing is often performed at elevated temperature. Modeling Mg and its alloys across the temperature range of interest is challenging and must account for the experimentally reported competition between compressive twins and pyramidal slip. Unfortunately, only few temperature-aware models for pure Mg and Mg alloys exist and many either disregard compressive twins entirely or suffer from efficiency or calibration issues, while experimental evidence of the active deformation modes has remained inconclusive. To describe the temperature-dependent behavior we introduce a new efficient, temperature-aware crystal-plasticity framework for pure Mg. Experimental stress–strain and texture data are used to calibrate the model over the range from room temperature to 300 °C. The calibrated model predicts single- and polycrystal stress–strain responses accurately in comparison with experimental data. By comparing two versions of the model – with and without compressive twins – we highlight their impact on the microstructure and texture evolution. Results highlight a transition in deformation modes from compressive twins at low temperature to pyramidal II slip at elevated temperature, confirming that the temperature dependence of pure Mg is primarily governed by non-basal slip. We thus provide an accurate and efficient modeling tool for the temperature-dependent mechanical behavior of pure Mg, while also shedding light onto the relative importance of non-basal slip vs. compressive twins as a function of temperature.

1. Introduction

Magnesium (Mg) is a light and abundant metallic material (Nie et al., 2020), which has an outstanding strength-to-weight ratio (competing with those of aluminum and titanium) and lends itself as a natural candidate for lightweight structural applications. Lightweight materials have further gained attention as a means to reduce the energy consumption of vehicles (the potential fuel savings from weight reduction could amount to around 9 g of CO_2 per km driven distance for every 100 kg of weight reduction in a vehicle) (Mordike and Ebert, 2001; Kulekci, 2008). Therefore, Mg is an ideal candidate for applications in the automotive and aerospace industry—in theory.

In practice, a number of fundamental drawbacks have prevented the wide usage of Mg and Mg alloys. Besides suffering from relatively low corrosion resistance, Mg-based materials are difficult to harden with conventional (thermal) methods (Eswarappa Prameela et al., 2021) and exhibit poor forming capabilities due to plastic anisotropy, a phenomenon linked to the
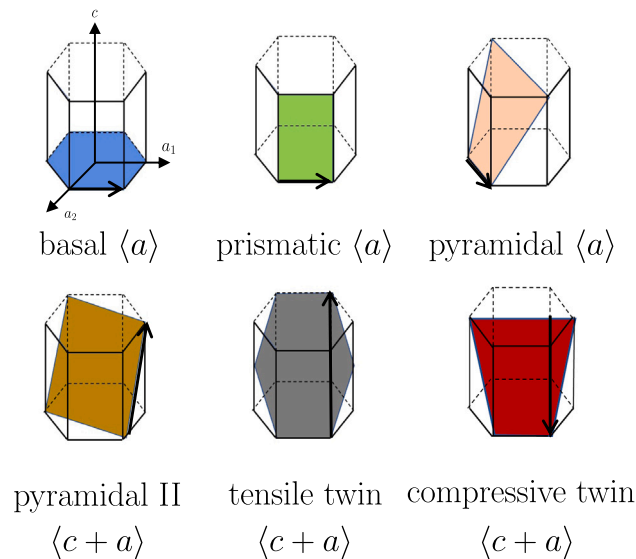

Fig. 1. Deformation modes of hcp metals: basal $\langle a \rangle$, prismatic $\langle a \rangle$, pyramidal $\langle a \rangle$, and second order pyramidal $\langle c + a \rangle$ slip as well as the two dominant twin systems, the $\{10\bar{1}2\}$ tensile twins (TT) and $\{10\bar{1}1\}$ compressive twins (CT).

hexagonal close-packed (hcp) atomic crystal structure, whose plastic behavior is the result of the collective activation of a variety of slip and twin mechanisms. Most commonly, basal, prismatic, and pyramidal slip systems as well as tensile and compressive twin systems (TT and CT, respectively) are observed, which are schematically shown in Fig. 1. For the sake of simplicity we will call the second order pyramidal $\langle c + a \rangle$ system the pyramidal II for short in all following instances. The disparate activation of deformation modes in the hcp system provides an insufficient number of activatable deformation modes required to accommodate plastic deformation at room temperature (Sandlöbes et al., 2011; Agnew et al., 2001; Staroselsky and Anand, 2003). This promotes the localization of plastic deformation in the twins, which in turn leads to the early onset of failure at room temperature (Kelley and Hosford, 1967; Nie et al., 2020; Wonsiewicz and Backofen, 1967). These shortcomings (and others, see e.g. Nie et al. (2020), Kecskes et al. (2021) or Eswarappa Prameela et al. (2021)) have prevented the wide-spread use of Mg alloys in industry.

Multiple approaches have increased the ductility and thus the workability of Mg, including the recent findings by Zeng et al. (2017), who showed that even pure Mg can become extremely malleable and ductile after undergoing severe grain refinement. The most common approach to improving the formability of Mg is to work at elevated temperature, which exploits the increased lattice mobility accompanying an increase in temperature, so that a larger number of deformation modes are available than at room temperature. This results in more homogeneous plastic deformation (Nie et al., 2020; Agnew and Duygulu, 2005; Barnett, 2007; Barnett et al., 2008; Sandlöbes et al., 2011; Ando et al., 2007; Chapuis and Driver, 2011; Kang et al., 2012), which in turn leads to a more isotropic and ductile behavior for improved workability and formability during processing. Mg alloys are thus often subjected to hot processing to overcome the aforementioned limitations (Wei et al., 2015; Zhou, 2016; Lee et al., 2002; Takuda et al., 1998; Mirzadeh, 2014). A detailed understanding of the thermo-mechanically coupled microstructure evolution – not to speak of a reliable predictive model – is still incomplete.

In order to understand the state of the art into which our model falls, we provide a brief review of presently available experimental data and models for the temperature-dependent plasticity of Mg and Mg alloys. Although we focus on pure Mg in this study, data for pure Mg is scarce, so that widely available data for Mg alloys is consulted, where required. For more exhaustive reviews, we refer to Nie et al. (2020) for a discussion of microstructure and properties of wrought Mg alloys, Sitdikov and Kaibyshev (2001) for a review of thermal and recrystallization effects in Mg and Mg alloys, and Kecskes et al. (2021), who provided a recent compilation of findings.

1.1. Experimental investigations

The plastic behavior of Mg and Mg alloys has been the subject of experimental studies for decades (Yoshinaga and Horiuchi, 1963; Kelley and Hosford, 1967; Wonsiewicz and Backofen, 1967; Yoo, 1981; Christian and Mahajan, 1995; Agnew and Duygulu, 2005; Sandlöbes et al., 2011; Akhtar and Teghtsoonian, 1969; Chapuis and Driver, 2011). It was observed that single-crystals and textured polycrystals show strong plastic anisotropy.

Single- and polycrystal experiments revealed that basal slip and TTs dominate at room temperature (Wonsiewicz and Backofen, 1967; Akhtar and Teghtsoonian, 1969; Kelley and Hosford, 1967; Zhang and Joshi, 2012; Nie et al., 2020), while the contributions of the various non-basal systems increase with increasing temperature (Yoshinaga and Horiuchi, 1963; Yoshinaga et al., 1973; Obara et al., 1973; Ono et al., 2004; Barnett et al., 2008; Reed-Hill and Robertson, 1957; Yoo and Wei, 1967; Burke and Hibbard, 1952;

Chapuis and Driver, 2011). Due to the reduced activation stresses on these systems, at elevated temperature, pyramidal and prismatic slip accommodate a larger portion of the plastic deformation. This leads to a smaller relative contribution of basal slip and twin systems to accommodate the overall deformation (Barnett, 2007; Kecskes et al., 2021; Nie et al., 2020). Hence, a strong temperature dependence of the non-basal slip systems was inferred, whereas, surprisingly, it was found that basal slip as well as TTs show little to no change in behavior with increasing temperature and are often assumed to be virtually temperature independent (Chapuis and Driver, 2011; Nie et al., 2020).

Although most studies confirm the above general trends, there exists contradictory experimental evidence and interpretation of the microstructure of Mg, both at room temperature and at elevated temperature. One such controversy lies in the presence of pyramidal II slip at room temperature. Ono et al. (2004), Muránsky et al. (2008), Koike et al. (2003) reported significant contributions of pyramidal slip starting at ambient temperature. Further, Lilleodden (2010) reported that only pyramidal II slip was active during their micro-compression studies, whereas Kelley and Hosford (1967), Wonsiewicz and Backofen (1967) found no evidence of this deformation mode. Another controversially discussed aspect is the role of the CT systems with increasing temperature. CTs have been observed in both single- and polycrystal studies at room temperature (Wonsiewicz and Backofen, 1967; Barnett, 2007; Barnett et al., 2008) and are considered one of the main reasons for the early failure of Mg alloys Al-Samman et al. (2010), Zhou and Sui (2019), Chakkedath et al. (2018). Their temperature dependence, however, has remained an open question. Wonsiewicz and Backofen (1967) observed an increasing amount of CTs in their single-crystal experiments at higher temperatures, whereas Barnett (2007), Barnett et al. (2008), Kecskes et al. (2021), Chakkedath et al. (2018) noted a reduced propensity for twinning and especially for CT with increasing temperature. To accommodate deformation along the c-axis of the crystal, the material must exhibit some deformation mode(s) with a c-component in the Burgers vector. Due to the polar nature of twinning, the $\{10\bar{1}2\}$ TT system can only do so under c-axis extension, and the $\{10\bar{1}1\}$CT systems only under compression. The nature of a twin system (tensile or compressive) is due to the c/a ratio of the material (Yoo, 1981). Pyramidal II systems, by contrast, can account for both types of deformation. Interestingly, this results in a competition between these aforementioned deformation modes. Understanding the nature of the controversial findings and the competition between the pyramidal II and the CT systems will, among others, be the subject of this investigation. Recently, the question was raised whether pyramidal I $\langle c + a \rangle$ or pyramidal II slip was the predominant mode: Kweon and Raja (2021), Zecevic et al. (2018), and Xie et al. (2016) suggested that pyramidal I $\langle c + a \rangle$ slip may be the dominant mode. Since, however, little is known about the temperature-dependent behavior of pyramidal I $\langle c + a \rangle$ slip, investigating this additional controversy lies outside the scope of this work.

1.2. Numerical studies

Thanks to the advent of inexpensive and accessible computational power, a steadily growing number of numerical techniques have been employed to improve our understanding of plasticity in hcp metals. Modeling occurs on a variety of length (and time) scales, from the atomic to the continuum level, each providing different insight and suffering from different limitations. Molecular Dynamics (MD) simulations have provided insight at the scale of lattice defects, including the formation of dislocations, twins, and voids as well as solute clustering in alloys (Yi et al., 2017, 2021; Hu et al., 2020; Wang et al., 2022). At larger scales, phenomenological models trade efficiency for accuracy and mechanistic rigor to allow for simulations of large, especially polycrystalline, systems. This includes primarily phase field and crystal plasticity models as well as combinations thereof (Liu et al., 2017, 2019a; Clayton and Knap, 2011; Staroselsky and Anand, 2003; Zhang and Joshi, 2012), which live at continuum scales. A noteworthy advance in the efficient representation of deformation twinning on larger scales is due to Tomé et al. (1991), who introduced the predominant twin reorientation model, capturing the texture change in zirconium due to twinning events and contributing significantly to the texture modeling of hcp materials.

In this study, we focus on continuum-level mesoscale modeling, which admits simulating large ensembles of grains, while being efficient and incorporating the underlying deformation modes to investigate the microstructure evolution. When adopting the nomenclature of Liu et al. (2017), phenomenological mesoscale approaches can be categorized as *top-down* (Ardeljan et al., 2016; Knezevic et al., 2009; Tam et al., 2020; Chen et al., 2020) and *bottom-up* (Chang and Kochmann, 2015; Liu et al., 2017; Zhang and Joshi, 2012; Kweon and Raja, 2021) based on the model calibration. Top-down approaches use experimental polycrystal data to calibrate the model parameters, whereas bottom-up approaches calibrate a single-crystal plasticity (SCP) model with available experimental data and use that SCP description locally in a polycrystalline simulation framework. In comparison, this latter approach shows superior accuracy and is applicable to general polycrystalline textures. As a bottom-up example, the variational SCP framework of Chang and Kochmann (2015) for pure Mg used a reduced set of active deformation mechanisms for an efficient representation of the Mg microstructure. When embedded in finite element (FE) (Chang et al., 2017) or Fast Fourier Transform (FFT) (Vidyasagar et al., 2018) homogenization schemes, this model was shown to efficiently predict the stress–strain behavior and texture evolution of polycrystals.

Both bottom-up and top-down approaches have proven successful in capturing essential features of Mg's plastic behavior. Ardeljan et al. (2016) captured the temperature and strain rate dependence of Mg alloy AZ31 in a multiscale "FE×Taylor" top-down framework. Further, Jain and Agnew (2007) successfully investigated the temperature effects on twinning in Mg alloy AZ31B by means of a top-down viscoplastic self-consistent model, and Walde and Riedel (2007) successfully modeled recrystallization in AZ31 with a similar approach. More recently, Tam et al. (2020) accurately modeled the temperature-dependent response of AZ31 polycrystals as well as the texture evolution and the dynamic recrystallization, while Sahoo et al. (2020) investigated the texture evolution in an all-twin-variant crystal plasticity model for hcp materials, capturing the twin effects and intersecting twin variants. Despite these successes, top-down approaches typically suffer from significant drawbacks, including a strong dependence on the

choice of the calibration data and of the homogenization method (Ardeljan et al., 2016), the inability to apply at the single-crystal level, and a lack of microstructural insight (Roy et al., 2017).

Despite the wealth of models for hcp materials, only a small number of temperature-dependent models for Mg exist. On the one hand, the bottom-up approach of Zhang and Joshi (2012) for the room-temperature description of Mg single- and polycrystals was adopted by Liu et al. (2017) and extended to the temperature range from 298 K to 523 K, observing a transition in deformation modes with increasing temperature. The latter was primarily associated with a decrease of basal slip at elevated temperature at the expense of pyramidal $\langle a \rangle$ slip as well as a transition from CT to pyramidal II slip with increasing temperature. On the other hand, (Wang et al., 2019) used a Johnson–Cook-type hardening law for single-crystals and included temperature dependence, while considering CTs as quasi-inactive at room temperature, while showing a transition away from pyramidal slip to CT above 423 K. The reported microstructures of both approaches were substantially different and to some degree contradictory. Furthermore, the assumptions made by Wang et al. (2019) on the behavior of CTs were not supported by the observations of Barnett (2007), Barnett et al. (2008). Both Wang et al. (2019) and Liu et al. (2017) included the entire range of possible deformation (slip and twin) modes. This choice is problematic from a calibration point of view, as, e.g., pyramidal $\langle a \rangle$ slip and prismatic slip, as well as pyramidal II slip and CTs are in direct competition, which may corrupt or at least exacerbate the calibration, even on the basis of single-crystal experiments, as noted by Zhang and Joshi (2012).

1.3. Scope of this work

The aim of this study is twofold: to provide a new and efficient temperature-dependent crystal plasticity model for Mg and to shed light onto the competition between pyramidal slip and CT systems and the thermally induced change in deformation mechanisms. To this end, we present two temperature-aware extensions of the SCP model of Chang and Kochmann (2015), which differ in the microstructural details. The first formulation, based on Chang and Kochmann (2015), incorporates a reduced representation with what we identified as a minimally viable number of deformation modes. This *reduced* model aims to overcome challenges linked to the calibration of model parameters and provides an easy-to-calibrate predictive model that captures the full range of temperature-dependent stress–strain behavior in a bottom-up scheme. The second formulation, the *full* model, extends Chang and Kochmann (2015) through the incorporation of the CT systems, offering a rigorous numerical investigation and aimed at better understanding the competition between pyramidal slip and CTs vs. temperature. Both models are integrated in a Taylor mean-field approach to predict the response of Mg polycrystals. This setup is finally used to investigate the evolution of texture during rolling and compression.

2. Crystal plasticity model

Our SCP model is an extension of the original formulations by Chang and Kochmann (2015), Vidyasagar et al. (2018), and Tutcuoglu et al. (2019b), which we summarize in the following to the extent necessary for subsequent discussions. As a novelty, we render the model temperature-dependent, and we modify the representation of the individual deformation modes.

2.1. Kinematics of slip and twin mechanisms in Mg

Let s_α and m_α denote the slip directions and normals of the N_p slip systems $\alpha \in [1, N_p]$, whereas a_β and n_β are the twinning directions and normals of the N_{tw} twin systems $\beta \in [1, N_{tw}]$. The total deformation gradient is assumed to follow a multiplicative decomposition into elastic and inelastic contributions (Kalidindi, 1998; Asaro and Rice, 1977), so

$$F = F_e F_{in}, \tag{1}$$

where F_e represents the elastic part, and F_{in} stems from the combined slip and twin activity of the respective systems. Note that the above choice of the decomposition is non-unique and other approaches exist, in which the deformation gradient is decomposed further into components for slip and twinning (Homayonifar and Mosler, 2011), resulting in the interactions of twin and slip activity at the kinematic level. In our case, the interaction between slip and twinning is embedded in the constitutive relations, as discussed in Section 2.2.

The total velocity gradient follows as

$$l = \dot{F} F^{-1}$$
$$= \underbrace{\dot{F}_e F_e^{-1}}_{l_e} + F_e \underbrace{\dot{F}_{in} F_{in}^{-1}}_{\tilde{l}_{in}} F_e^{-1}, \tag{2}$$

with elastic and inelastic contributions l_e and $\tilde{l}_{in}$, respectively. The latter is further decomposed into slip and twin components:

$$\tilde{l}_{in} = \tilde{l}_p + \tilde{l}_{tw}, \tag{3}$$

where $\tilde{l}_{tw}$ results from the combined effect of the changing N_{tw} twin volume fractions λ_β. With γ_β^{tw} denoting the twinning shear strain (a material constant known from the crystallography (Zhang and Joshi, 2012)) associated with system β, this implies

$$\tilde{l}_{tw} = \sum_{\beta=1}^{N_{tw}} \dot{\lambda}_\beta \gamma_\beta^{tw} a_\beta \otimes n_\beta. \tag{4}$$

$\tilde{l}_{\mathrm{p}}$ stems from the activities of the slip systems in the twinned and untwinned regions of the crystal, so that

$$\tilde{l}_{\mathrm{p}} = \sum_{\alpha=1}^{n_s} \dot{\gamma}_\alpha \underbrace{\left[\left(1 - \sum_{\beta=1}^{N_{\mathrm{tw}}} \lambda_\beta \right) s_\alpha \otimes m_\alpha + \sum_{\beta=1}^{N_{\mathrm{tw}}} \lambda_\beta s'_\alpha \otimes m'_\alpha \right]}_{=p_\alpha} . \tag{5}$$

Here, the slip rates $\dot{\gamma}_\alpha$ are assumed to capture slip in both untwinned and fully twinned regions, the latter being defined for twin system β by

$$s'_\alpha = Q_\beta s_\alpha; \quad m'_\alpha = Q_\beta m_\alpha. \tag{6}$$

with the householder mapping

$$Q_\beta = I - 2n_\beta \otimes n_\beta, \tag{7}$$

which describes the reorientation of the lattice due to the twinning of the crystal around the plane normal of system β (Christian and Mahajan, 1995).

2.2. Constitutive relations

Following Chang and Kochmann (2015), we introduce the Helmholtz free energy density, here dependent on temperature T, as

$$W(F, F_{\mathrm{in}}, \epsilon, \lambda, T) = W_{\mathrm{e}}(F_{\mathrm{e}}, T) + W_{\mathrm{p}}(\epsilon, \lambda, T) + W_{\mathrm{tw}}(\lambda, T), \tag{8}$$

consisting of a (hyper-)elastic energy density W_{e} and the stored plastic energies (i.e., energy irreversibly stored in the microstructure) due to slip and twinning, W_{p} and W_{tw}, respectively. The latter two depend on the twin volume fractions $\lambda = \{\lambda_1, \ldots, \lambda_{N_{\mathrm{tw}}}\}$ and the accumulated plastic strains $\epsilon = \{\epsilon_1, \ldots, \epsilon_{N_{\mathrm{p}}}\}$, which evolve according to $\dot{\epsilon}_\alpha = |\dot{\gamma}_\alpha|$, $\dot{\gamma}_\alpha$ being the slip rate on system α.

The twin and slip contributions to the energy density account for self- and latent hardening. We base our description of the twin hardening on Chang and Kochmann (2015), Tutcuoglu et al. (2019b), while incorporating the CT effect similar to Zhang and Joshi (2012), assuming they follow the same Schmid-type behavior as TTs.[1] The hardening of TTs and CTs is assumed to follow a linear law, which leads to

$$W_{\mathrm{tw}} = \underbrace{\sum_{\beta=1}^{n_t} \frac{k_\beta(T)}{2} \lambda_\beta^2}_{\text{self-hardening}} + \underbrace{\frac{1}{2} \lambda \cdot \mathcal{K}(T) \lambda}_{\text{cross-hardening}} , \tag{9}$$

whereas plastic hardening due to slip is based on

$$W_{\mathrm{p}} = \begin{cases} \underbrace{\sum_{\alpha=1}^{n_s} \sigma_\alpha^\infty(T) \left[\epsilon_\alpha + \frac{\sigma_\alpha^\infty(T)}{h_\alpha^0(T)} \exp\left(-\frac{h_{0,\alpha}(T)\epsilon_\alpha}{\sigma_\alpha^\infty(T)} \right) \right]}_{\text{self-hardening}} + \underbrace{\frac{1}{2} \epsilon \cdot \mathcal{H}(T) \epsilon}_{\text{cross-hardening}}, & \text{if } \lambda < \lambda_{\mathrm{crit}}, \\[3em] \underbrace{\sum_{\alpha=1}^{n_s} \sigma_\alpha^\infty(T) \left[\epsilon_\alpha + \frac{\sigma_\alpha^\infty(T)}{h_\alpha^0(T)} \exp\left(-\frac{h_{0,\alpha}(T)\epsilon_\alpha}{\sigma_\alpha^\infty(T)} \right) \right]}_{\text{self-hardening}} + \underbrace{\frac{1}{2} \epsilon \cdot \mathcal{H}(T) \epsilon}_{\text{cross-hardening}} + \underbrace{\sum_{\alpha=1}^{N_s} c_\alpha(T) \epsilon_\alpha}_{\text{twin-slip interaction}}, & \text{if } \lambda \geq \lambda_{\mathrm{crit}}. \end{cases} \tag{10}$$

$\mathcal{K}$ is a positive semi-definite matrix, having twin cross-hardening terms $k_{\beta\beta'}$ in its off-diagonal components and a zero diagonal to represent twin–twin cross-hardening. Specifically, the values of $k_{\beta\beta'}$ are chosen such as to admit only one active (compressive or tensile) twin variant at a time (Chang and Kochmann, 2015). Analogously, $\mathcal{H}(T)$ is a positive semi-definite matrix, capturing slip–slip cross-hardening through terms $h_{\alpha\alpha'}$ on its off-diagonals and a zero diagonal.

Twin hardening effects on the slip systems are included via a saturation hardening law. Upon reaching a critical twin volume fraction, the twin is considered saturated and set to be fully reoriented. This leads to strain hardening (Kecskes et al., 2021) (due to twin boundary and geometric hardening, while the Basinski effect leads to the transformation of glissile into sessile dislocations (Knezevic et al., 2010; Basinski et al., 1997)). As we do not resolve twins spatially nor account for the formation of twin lamellae (such as, e.g., in the composite grain model of Proust et al. (2007)), these effects are condensed into a single hardening parameter c_α, applied upon twin saturation. Jain and Agnew (2007) noted that not all systems are affected equally by the presence of twins, which is why their model introduced a stronger latent hardening factor for basal slip. Similar observations were made by Yu et al. (2018), who investigated experimentally the hardening effect of twinning on basal and prismatic slip in

---

[1] It was noted as early as by Kelley and Hosford (1967) that CTs may in fact *not* follow this pattern. In modeling, however, when included, CTs are generally assumed to follow approximately a Schmid law with a medium to high critical resolved shear stress (CRSS) value and strong hardening (Zhang and Joshi, 2012; Wang et al., 2019; Liu et al., 2017). For the sake of simplicity we here follow this assumption—investigating the physics behind CTs goes beyond the scope of this contribution and requires lower-scale models of experimental insight.

AZ31, noticing an increased effect of twin hardening on basal systems as compared to prismatic systems. Here, this phenomenon is accounted for by different choices for the parameters c_α in (10).

Assuming that both slip and twinning follows a Schmid-type law, the resolved shear stress (RSS) of slip system α is

$$\tau_\alpha^{\mathrm{p}} = \boldsymbol{\Sigma} \cdot \boldsymbol{p}_\alpha, \tag{11}$$

with $\boldsymbol{p}_\alpha$ from (5). Equivalently, the RSS for twin system β becomes

$$\tau_\beta^{\mathrm{tw}} = \boldsymbol{\Sigma} \cdot \gamma_\beta^{\mathrm{tw}} \boldsymbol{a}_\beta \otimes \boldsymbol{n}_\beta, \tag{12}$$

with the Mandel stress tensor $\boldsymbol{\Sigma}$, defined as

$$\boldsymbol{\Sigma} = \boldsymbol{F}_{\mathrm{e}}^T \boldsymbol{P} \boldsymbol{F}_{\mathrm{in}}^T \quad \text{with} \quad \boldsymbol{P} = \frac{\partial W}{\partial \boldsymbol{F}}. \tag{13}$$

The evolution laws for the plastic slips in this variational setting follow as

$$\dot{\gamma}_\alpha = \dot{\gamma}_{0,\alpha} \left| \frac{|\tau_\alpha^{\mathrm{p}}| - \frac{\partial W_{\mathrm{p}}}{\partial \epsilon_\alpha}}{\tau_{0,\alpha}(T)} \right|^{1/m_{\mathrm{p}}} \mathrm{sign}(\tau_\alpha^{\mathrm{p}}), \tag{14}$$

with reference slip rates $\dot{\gamma}_{0,\alpha}$, a temperature-dependent CRSS $\tau_{0,\alpha}$ for each slip system, and hardening exponent m_{p}. Analogously, the twin volume fractions evolve according to

$$\dot{\lambda}_\beta = \dot{\lambda}_{0,\beta} \left| \frac{|\tau_\beta^{\mathrm{tw}}| - \frac{\partial W_{\mathrm{tw}}}{\partial \lambda \beta}}{\tau_{0,\beta}} \right|^{1/m_{\mathrm{tw}}} \tag{15}$$

with a reference rate $\dot{\lambda}_{0,\beta}$, hardening exponent m_{tw}, and temperature-independent CRSS $\tau_{0,\beta}$.

The constitutive model is completed by a choice of the elastic energy density. Chang and Kochmann (2015) showed that – owing to its low level – elastic anisotropy has a negligible effect on the texture evolution and stress–strain relation of Mg. For simplicity, we thus choose a compressible Neo-Hookean strain energy density

$$W_{\mathrm{e}}(\boldsymbol{F}_{\mathrm{e}}, T) = \frac{\mu(T)}{2}(\mathrm{tr}\,\bar{\boldsymbol{C}}_{\mathrm{e}} - 3) + \frac{\kappa(T)}{2}(J - 1)^2 \tag{16}$$

with

$$\bar{\boldsymbol{C}}_{\mathrm{e}} = \bar{\boldsymbol{F}}_{\mathrm{e}}^T \bar{\boldsymbol{F}}_{\mathrm{e}}, \quad \bar{\boldsymbol{F}}_{\mathrm{e}} = \frac{\boldsymbol{F}_{\mathrm{e}}}{J^{1/3}}, \quad J = \det \boldsymbol{F}_{\mathrm{e}} = \det \boldsymbol{F} \tag{17}$$

and temperature-dependent shear and bulk moduli μ and κ, respectively.

2.3. Temperature dependence

The temperature dependence of slip and twinning was studied, among others, by Chapuis and Driver (2011), Wonsiewicz and Backofen (1967), who concluded that basal slip and tensile twins are largely temperature insensitive, whereas non-basal slip and compressive twins (CT) show a moderate to strong temperature dependence—as also argued by Liu et al. (2017), Wang et al. (2019), Nie et al. (2020).

We note that some studies observed reduced twin activity with increasing temperature (Kecskes et al., 2021; Jain and Agnew, 2007; Wonsiewicz and Backofen, 1967; Chapuis and Driver, 2011), which can be explained by the fact that other deformation modes can more readily accommodate the deformation due to the increased lattice mobility, leading to a reduction in twinning. Further, the accrued slip may have an inhibitory effect on twinning. Jain and Agnew (2007) assumed an *inverse* temperature dependence of the CRSS of TT systems in their study of AZ31, leading to hardening and a reduction of twin activity with increasing temperature. Although that assumption does yield the expected result of a decrease in twin activity at elevated temperature, it is questionable, whether the phenomenon they observed is due to an actual increase in the CRSS value or due to other effects, such as the increased propensity for precipitates in the alloy, which are known to promote twin hardening (Liu et al., 2019b). As the present formulation of the model cannot account for complex mechanistic effects, we follow Chapuis and Driver (2011), Wonsiewicz and Backofen (1967) and assume that the TT (and basal slip) systems are temperature-independent, so that temperature dependence is incorporated only in the non-basal slip systems, and in CTs, as in Liu et al. (2017), Wang et al. (2019).

Similar to Beyerlein and Tomé (2004), Liu et al. (2017), Wang et al. (2019), we assume an Arrhenius-type law for the temperature dependence of the CRSS values, so the temperature dependence of the non-basal slip systems is assumed to decay exponentially with temperature, i.e.,

$$\tau_{0,\alpha}(\bar{T}) = \begin{cases} \tau_{0,\alpha}(T_{\mathrm{ref}}) & \text{for basal systems,} \\ \tau_{0,\alpha}(T_{\mathrm{ref}}) \exp(-\omega_\alpha \bar{T}) & \text{else,} \end{cases} \tag{18}$$

with distinct parameters $\omega_\alpha > 0$ for the prismatic and pyramidal systems, and the dimensionless temperature

$$\bar{T}(T) = \frac{T - T_{\mathrm{ref}}}{T_{\mathrm{melt}} - T_{\mathrm{ref}}}. \tag{19}$$

The melting temperature of Mg is $T_{\text{melt}} = 650\ °C$, while we take as a reference the ambient temperature $T_{\text{ref}} = 25\ °C$.

The exponential ansatz is also used to describe the temperature sensitivity of the Voce hardening parameters:

$$h_\alpha^0(\bar{T}) = \begin{cases} h_\alpha^0(T_{\text{ref}}) & \text{for basal systems,} \\ h_\alpha^0(T_{\text{ref}}) \exp(-\eta_\alpha \bar{T}) & \text{else,} \end{cases}$$

$$h_{\alpha\alpha'}(\bar{T}) = \begin{cases} h_{\alpha\alpha'}(T_{\text{ref}}) & \text{for basal systems,} \\ h_{\alpha\alpha'}(T_{\text{ref}}) \exp(-\chi_\alpha \bar{T}) & \text{else,} \end{cases} \tag{20}$$

$$\sigma_\alpha^\infty(\bar{T}) = \begin{cases} \sigma_\alpha^\infty(T_{\text{ref}}) & \text{for basal systems,} \\ \sigma_\alpha^\infty(T_{\text{ref}}) \exp(-\nu_\alpha \bar{T}) & \text{else.} \end{cases}$$

Analogously, the hardening laws for TTs are assumed to be temperature insensitive:

$$k_\beta^0(\bar{T}) = \begin{cases} k_\beta(T_{\text{ref}}) & \text{for TT systems} \\ k_\beta(T_{\text{ref}}) \exp(-\xi_\beta \bar{T}) & \text{for CT systems.} \end{cases} \tag{21}$$

The entries of $\mathcal{K}$ are temperature-*independent*. The twin–twin cross hardening matrix ensures no more than one twin system is active at the material point. This assumption does not collapse for elevated temperatures. Finally, the elastic constants are chosen as $\mu(T) = 17 \exp(-3\bar{T})$ GPa and $\kappa(T) = 16 \exp(-3\bar{T})$ GPa, by extending the (room-temperature) Neo-Hookean formulation from Vidyasagar et al. (2018).

2.4. Taylor model for polycrystal simulations

A simple mean-field, Taylor-type homogenization scheme is adopted to represent polycrystals in a highly efficient and parallelizable fashion. We note that, while efficiency is one of this method's key strengths, the Taylor model does not have an intrinsic length scale and does not account for detailed spatial variations on the grain level. Those could be captured by a (significantly more expensive) spatially-resolved model (Chang and Kochmann, 2015; Vidyasagar et al., 2018). The present model aims to efficiently provide an estimate for the effective, macroscale response of a large ensemble of grains on the microscale. We thus consider an ensemble of N grains on the microscale, each given a volume fraction $f_i \in [0, 1]$.

Furthermore, each grain is endowed with an initial crystallographic orientation, described by a 3D rotation tensor $R_i \in \text{SO}(3)$, which defines the slip and twin systems within grain i in the global coordinate system as, respectively,

$$s_{i,\alpha} = R_i s_\alpha, \qquad m_{i,\alpha} = R_i m_\alpha, \tag{22}$$

and

$$n_{i,\beta} = R_i n_\beta, \qquad a_{i,\beta} = R_i a_\beta. \tag{23}$$

With each grain having internal variables $\eta = [\epsilon, \lambda]$, we denote the set of all internal variables in the polycrystal by $\mathcal{G} = \{\eta_1, f_1, \ldots, \eta_N, f_N\}$, and the set of all grain orientations is $\mathcal{R} = \{R_1, \ldots, R_N\}$.

Following the Taylor assumption, each grain is subject to the same applied deformation gradient F (hence expecting an upper bound on the effective, homogenized polycrystal response), see Fig. 2 for a visualization. We furthermore assume a uniform, constant temperature T across the polycrystal (thus neglecting the heat generated by plastic mechanisms under quasistatic loading). With the individual grain behavior given by the single-crystal model of Sections 2.1–2.3, the response of the polycrystal is obtained from the volume fraction-weighted grain average, so the effective energy density reads

$$W_{\text{Taylor}}(F, \mathcal{R}, \mathcal{G}) = \sum_{i=1}^N f_i W(R_i F, \epsilon_i, \lambda_i), \tag{24}$$

and the effective first Piola–Kirchhoff stress tensor follows as

$$P = \frac{\partial W_{\text{Taylor}}}{\partial F}. \tag{25}$$

3. Parameter identification and model validation

Our (bottom-up) strategy is to first calibrate the *room-temperature single-crystal* model, followed by calibrating the *temperature-related* parameters, for both of which the Taylor model provides *poly-crystal* predictions for validation. We begin by calibrating the room-temperature single-crystal model, using the data reported by Kelley and Hosford (1967), who performed a series of room-temperature channel-die experiments. They used seven distinct orientations of their single-crystal samples with respect to the applied loading, denoted by cases A through G, which were designed to isolate the behavior of individual slip and twin systems in Mg at room temperature. Table 1 provides an overview of the applied deformation and constraints as well as the deformation mechanism(s) calibrated by each case.
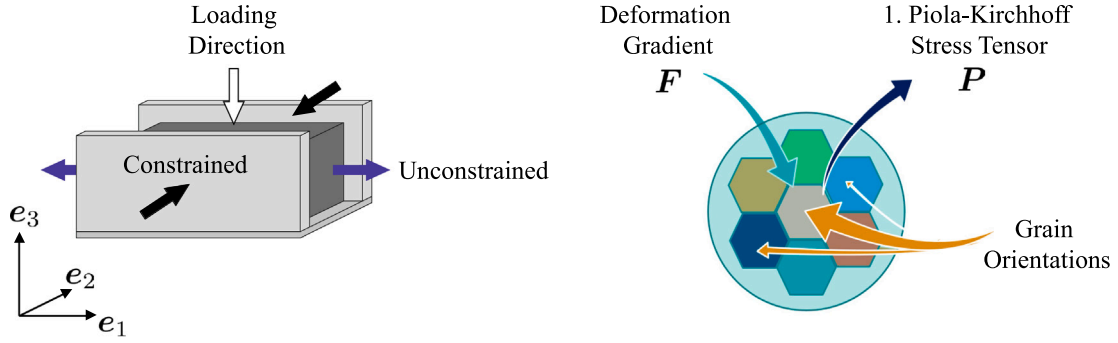
Fig. 2. Schematic view of the Taylor model used for the extraction of the polycrystal response during channel-die loading with the indicated loading, constraint, and unconstrained free directions.

Table 1

The seven cases in the channel-die experiments of Kelley and Hosford (1967). Single-crystals were subjected to plane-strain compression, being compressed in the *Compression* direction with a rigid constraint imposed in the *Constraint* direction, while being unconstrained in the third (orthogonal) direction. Each case is designed to promote the activity of the denoted system (*Deform. Mode(s)*), including pyramidal (Py), prismatic (Pris) and basal slip as well as tension twins (TT) and compressive twins (CT).

Case	A	B	C	D	E	F	G
Compression	$\{0001\}$	$\{0001\}$	$\{10\bar{1}0\}$	$\{1\bar{2}10\}$	$\{10\bar{1}0\}$	$\{1\bar{2}10\}$	$\{0001\}$ @ 45°
Constraint	$\{10\bar{1}0\}$	$\{1\bar{2}10\}$	$\{0001\}$	$\{0001\}$	$\{1\bar{2}10\}$	$\{10\bar{1}0\}$	$\{10\bar{1}0\}$
Deform. Mode(s)	Py & CT	Py & CT	Pris & CT	Pris & CT	TT	TT	Basal

Simulations for calibration were performed under quasistatic conditions at a strain rate of $\dot{\epsilon} = 10^{-4}\text{s}^{-1}$. The channel-die setup—with compression being applied in the x_3-direction and the sample surfaces perpendicular to the x_1-direction left free and constrained in the x_2-direction, is approximated by imposing the deformation gradient

$$\boldsymbol{F} = \begin{pmatrix} F_{11} & F_{12} & F_{13} \\ 0 & 1 & 0 \\ 0 & 0 & e^{\dot{\epsilon}t} \end{pmatrix}. \tag{26}$$

The unknown entries F_{1i} (accounting for the free boundaries of the channel) are found by solving for the traction-free boundary conditions $P_{1i} = 0$ (Chang, 2016).

Parameter calibration starts with the room-temperature CRSS values, which were chosen to lie in the range reported experimentally (see Fig. 3), with the parameters reported by Chang and Kochmann (2015) used as initial guess. The room-temperature CRSS values were, once chosen, held constant for the remainder of the calibration process.

The calibration for each case in Table 3 (assuming that only the indicated deformation modes are active) follows the same protocol. With the Voce hardening laws, the initial onset of plastic flow is governed by the CRSS values of the active systems. The peak stress depends mostly on the saturation stress σ_α^∞, while the shape of the plastic stress–strain curve depends primarily on the self-hardening factor h_α^0. The large-strain behavior additionally depends on the cross-hardening factors $h_{\alpha\alpha'}$ and h_α^0. Calibration of the model was accomplished by critically comparing the results of the simulated single-crystal behavior to the experimental stress–strain data of Kelley and Hosford (1967), calibrating the relevant model parameters one at a time to capture the onset of plastic flow, hardening, and large-strain behavior in a similar spirit to Zhang and Joshi (2012).

This procedure works best when there is no ambiguity in the deformation modes during plastic deformation. Hence, Case G, involving only basal slip, proves easiest to calibrate, so optimal material parameters were readily obtained. Analogously, case E is ideally suited to calibrate the TT systems. Since twins follow a slightly different hardening law than the slip systems, hardening parameter k_0 was calibrated with the initial response of the single-crystal experiments from Kelley and Hosford (1967) to fit the slope of the twin hardening region up to 6% strain. The bifurcation point, indicating the saturation of the twin system and the subsequent reorientation of the lattice, corresponds to the results obtained by Zhang and Joshi (2012) for a critical volume fraction of 0.9.

Calibration of the pyramidal II and prismatic systems was less trivial, as both systems in principle occur simultaneously in cases A and C (along with CT). As a simplifying assumption, we assume that simulations of case A are dominated by pyramidal II slip and CT activity, and case C by the prismatic systems and CTs (as indicated in Fig. 3). This led to a iterative calibration route of those systems. Cases B and D, which feature the same deformation modes but to different extent, were used to check and validate the calibrated model parameters.

While in the reduced model (without CT) the seven cases were well suited to isolate each deformation mode, the ambiguity linked to the presence of the CT systems in the full model led to challenges (similar challenges were noted by Zhang and Joshi (2012)). As
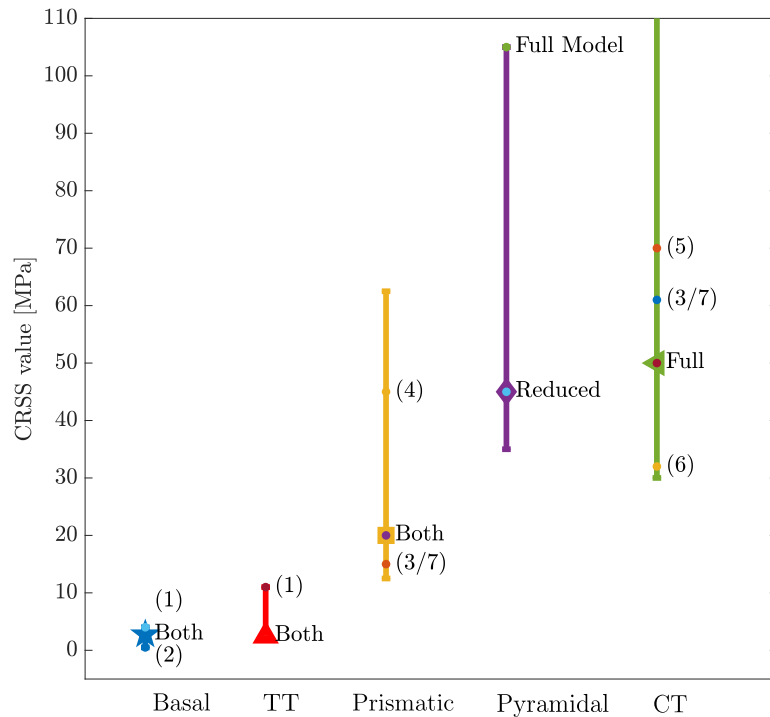
Fig. 3. Range of the experimentally reported CRSS values for the slip and twin systems. The shown ranges were obtained from Wang et al. (2019) and expanded with experimental data from Chapuis and Driver (2011)(1), Kelley and Hosford (1967)(2), Yoshinaga and Horiuchi (1963, 1964)(3,7), Akhtar and Teghtsoonian (1969)(4), Wonsiewicz and Backofen (1967)(5), and Kitahara et al. (2007)(6). The pyramidal II CRSS of the reduced model coincides with the experimental values of Obara et al. (1973).

a remedy, we assume, based on data from Kelley and Hosford (1967), Wonsiewicz and Backofen (1967), Yoshinaga and Horiuchi (1963), and Kitahara et al. (2007), that CTs exhibit a lower CRSS than the pyramidal II systems at lower temperatures. In fact, in the full model this assumption was necessary to obtain CT contributions in the first place. The self-hardening factor k_{CT}^0 of the CT systems was calibrated such as to capture the initial slope of case A, see Fig. 9. The excessive self-hardening is in agreement with experimental observations and simulation results (Wonsiewicz and Backofen, 1967; Zhang and Joshi, 2012). Upon saturation (not due to reaching the critical volume fraction, but instead due to extensive self-hardening) additional deformation is accommodated by pyramidal II slip.

Once calibrated at room temperature, the single-crystal model was made temperature-dependent, as described in Section 2.3, again beginning with the CRSS values, for which an exponential ansatz was chosen for the pyramidal II and prismatic $\langle a \rangle$ slip as well as the CT systems (see Section 2.3). Unfortunately, the experimentally reported CRSS values are inconclusive. For instance, the CRSS values for the prismatic systems reported by Yoshinaga and Horiuchi (1963) and Akhtar and Teghtsoonian (1969) differ substantially. The exponential decay parameters were thus obtained by critically comparing the predicted CRSS values with the range of experimental results reported by Chapuis and Driver (2011), Obara et al. (1973), Akhtar and Teghtsoonian (1969), Yoshinaga and Horiuchi (1963), Nie et al. (2020). Due to the wide range of experimental data, we note that the calibrated CRSS values may not represent physical material constant. We observe, however, good agreement with the experimentally reported values for the temperature range up to 300 °C, see Fig. 4.

Calibration of the hardening parameters at elevated temperature was performed via optimization, using the Nelder–Mead optimization routine from the SciPy library (Jones et al., 2001). For each case, an initial guess was chosen manually. As in the room-temperature case, the calibration of these systems is not straight-forward, and cases A and B need to be considered jointly. Therefore, in the numerical optimization, the objective was to minimize the mean square error (MSE) of the accumulated stress–strain error of both cases (A and C) at temperatures of $116°C$, $200°C$, $271°C$ for case A, and $110°C$, $180°C$, and $270°C$ for case C. This allowed us to identify the temperature parameters η_α, ξ_α, and ν_α for each deformation mode. Note that no global optimum was found, and the temperature-dependence depends on the initial guess. The optimization procedure was repeated 20 times, and the best set of parameters (in terms of the lowest stress–strain MSE) was chosen.

The calibration of the temperature parameters proved to be complex, since the room temperature data for cases A, B, C, and D from Kelley and Hosford (1967) and Wonsiewicz and Backofen (1967) differ significantly (see Fig. 5). While both authors reported similar peak stresses and general behavior, the path to failure varied. Data from Kelley and Hosford (1967) shows strong initial hardening in the elastic region with a flow stress of around 100 MPa, followed by a slow transition into a peak-stress around 300 MPa at 4% strain. The behavior reported by Wonsiewicz and Backofen (1967) exhibits a different initial hardening behavior:

Table 2

Model parameters for the slip systems at room temperature, calibrated based on the experimental data of Kelley and Hosford (1967). All values are for the reduced model, unless those marked by †, which are for the full model including the CT systems. Values marked by an asterisk (*) were calibrated based on data from Chapuis and Driver (2011), Akhtar and Teghtsoonian (1969), Lilleodden (2010), Ando et al. (2007), Kelley and Hosford (1967) The temperature dependence of the CRSS values was calibrated such as to lie in the range of experimentally reported data, see Fig. 4.

| Parameter	Symbol	Unit	Basal	Prismatic	Pyramidal II	Reference/Calibration
CRSS	τ_0	MPa	2.0	20	40 (100†)	calibration*
Self hardening factor	h_0	MPa	750	6000	13000	calibration
Cross hardening factor	h_{ij}	MPa	10	10	12	calibration
Saturation stress	σ^∞	MPa	0.8	72	115 (60†)	calibration
Twin-slip cross-hardening factor	c_α	MPa	20	10	5	calibration
Reference slip rate	$\dot\gamma_0$	s^{-1}	10^{-3}	10^{-3}	10^{-3}	Zhang and Joshi (2012)
Slip exponent	m_p	–	0.5	0.5	0.5	Chang and Kochmann (2015)
CRSS temperature factor	ω	–	–	3.0	2.95 (5.5†)	calibration*
Self-hardening temperature factor	η	–	–	5.2	4.5 (2.2†)	optimization
Cross-hardening temperature factor	ν	–	–	1.3	2.5	optimization
Saturation stress temperature factor	ξ	–	–	2.5	4.05 (2.5†)	optimization
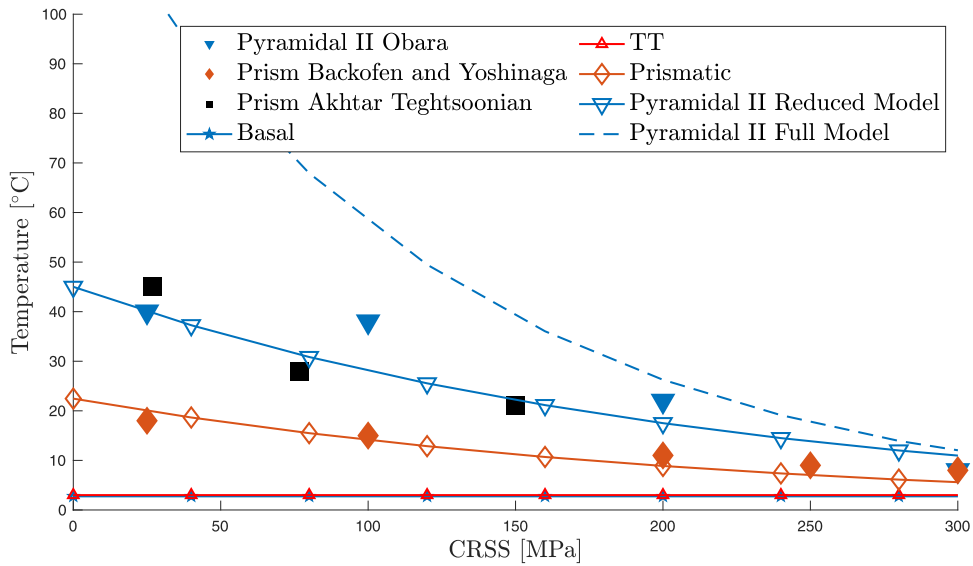
Fig. 4. Experimentally measured CRSS values for the slip and TT systems in Mg in comparison with this model over the studied range of temperatures. The filled markers show experimentally reported data from Obara et al. (1973), Wonsiewicz and Backofen (1967), Yoshinaga and Horiuchi (1964), Akhtar and Teghtsoonian (1969). The solid lines with markers represent the data for the reduced model, the dashed lines for the full model. The TT and basal CRSS values were constant for both models.

Table 3

Model parameters for the twin systems in full and reduced models, calibrated based on the data of Kelley and Hosford (1967), Wonsiewicz and Backofen (1967).

| Parameter	Symbol	Unit	TT	CT	Reference/Calibration
CRSS	τ_0	MPa	3.5	50	calibration
Self hardening factor	k_0	MPa	25	3000	calibration
Twin shear	$\dot\gamma_0$	–	0.129	1.066	Zhang and Joshi (2012), Chang and Kochmann (2015)
Cross hardening factor	h_{ij}	MPa	100	100	Chang and Kochmann (2015)
Critical volume fraction	υ_{crit}	–	0.9	0.9	Zhang and Joshi (2012)
Twin rate	$\dot\gamma_0$	–	10^{-3}	10^{-4}	Zhang and Joshi (2012)
Twin exponent	m_{tw}	–	1	1	Chang and Kochmann (2015)
CRSS temperature factor	ω	–	–	3.5	calibration
Self-hardening temperature factor	ξ	–	–	4.0	calibration
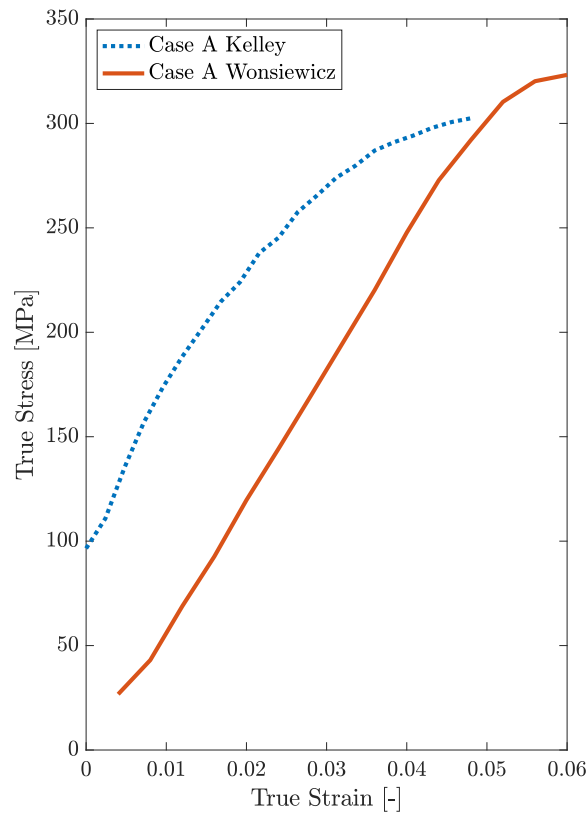
Fig. 5. Stress–strain data for the channel-die experiments of Kelley and Hosford (1967) (dotted line) and Wonsiewicz and Backofen (1967) (solid line).

the material seems to exhibit an early onset of plastic flow at considerably lower stresses of around 40 MPa, followed by slower and less pronounced hardening, which abruptly plateaus at around 5.5% strain before fracture occurs at 6% strain. We show a comparison for case A in Fig. 5, but the same trends persist for cases B, C, and D. While the differences in experiments rendered the calibration task more challenging, the fact that the peak stresses appear to be unaffected by the difference in experimental setups, the model was calibrated to the available single-crystal data despite the apparent differences. This calibration required manual tuning, as the optimizer generally tends to over-predict the stress at elevated temperature and under-predict at lower temperatures.

4. Single-crystal simulations

The single-crystal response of Mg is highly sensitive to the crystal orientation with respect to the applied loading, and it depends on temperature. Unfortunately, the literature is controversial when it comes to the non-basal slip vs. twin activity. Compression along the *c*-axis requires the activation of deformation modes such as pyramidal II slip or CTs (Yoshinaga and Horiuchi, 1963; Yoshinaga et al., 1973; Obara et al., 1973). According to Ono et al. (2004), $\langle c + a \rangle$ pyramidal slip is a prominent deformation mode for through-thickness compression along the *c*-axis. In a similar spirit, Koike et al. (2003), Muránsky et al. (2008), Obara et al. (1973) reported pyramidal II slip activity at room temperature. These findings stand in contradiction to the observations of Kelley and Hosford (1967), Wonsiewicz and Backofen (1967), who observe mostly $\{10\bar{1}1\}$ CTs and $\{10\bar{1}2\}$ TTs alongside large amounts of basal slip at room temperature and, in part, at elevated temperature, where especially the presence of TTs appears counter-intuitive due to the polar nature of the twin systems. With increasing temperature, Wonsiewicz and Backofen (1967) further observed increasing amounts of twinning and double twinning in Mg single-crystals, when compressed along the *c*-axis. This, in turn, is in contradiction to the more recent investigations by Barnett (2007), who found CT activity to be inversely proportional to temperature. Above a transition temperature, CTs were found to be less dominant, while non-basal slip systems account for the increasing amount of deformation (Barnett et al., 2008). Similar findings were reported by Khosravani et al. (2013) for alloy AZ31B, where this transition temperature was found to be as low as 350K. Wonsiewicz and Backofen (1967) reported evidence of CTs even at room temperature for cases C and D, in which the crystal is not ideally oriented for CTs to show activity. With the goal of shedding light into these controversial reports (while also validating the model's suitability), we proceed to model the response of Mg single-crystals, using the two versions of our model (reduced and full, where only the latter accounts for CT) along with a detailed comparison and discussion—and we do so both a room temperature and at elevated temperature.
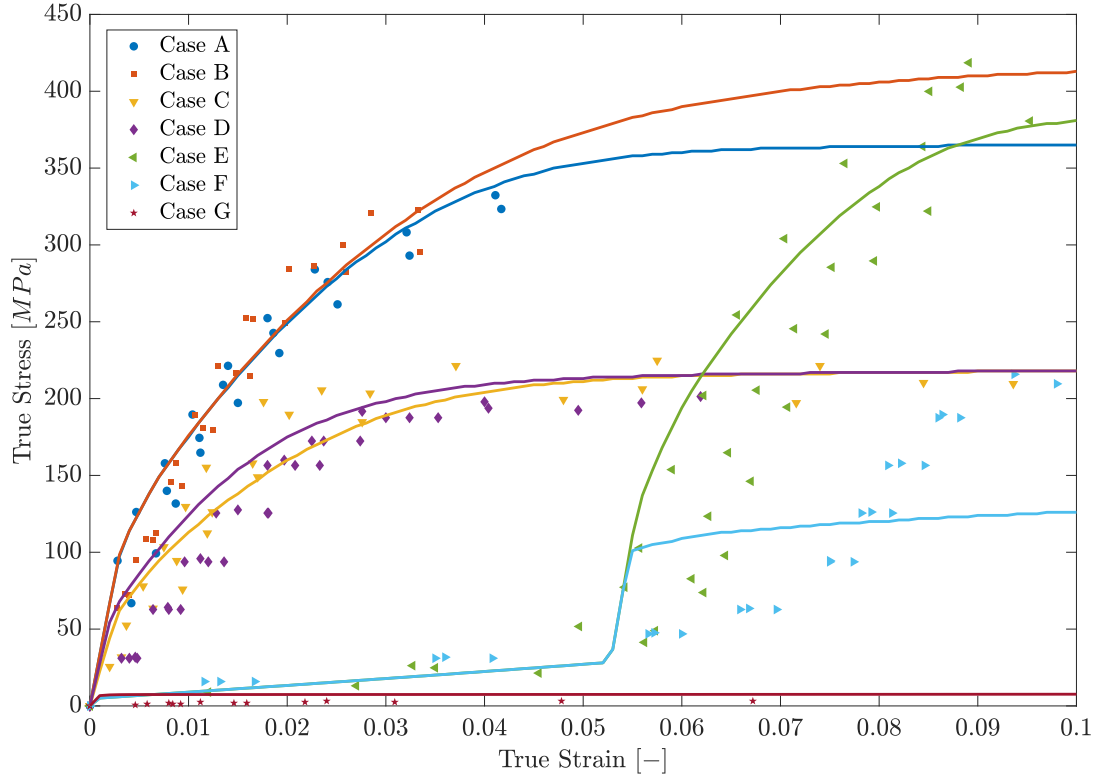
Fig. 6. Stress–strain responses of cases A through G. Dots represent experimental data by Kelley and Hosford (1967), solid lines are results simulated with the reduced model.

4.1. Room-temperature single-crystal response

4.1.1. Reduced representation (without CT)

Fig. 6 shows the stress–strain behavior of Mg single-crystals for cases A through G, predicted by the reduced model with the material parameters in Table 2. The predicted response captures the salient features and compares well with the experimental data in all cases. To highlight the microstructure evolution, we also report the predicted activity of the various deformation modes. To this end and to compare the activities, we introduce as a qualitative measure the *relative activity of each deformation mode* as

$$\mathcal{Y}_{\text{bas./prism./pyr.}} = \frac{\Gamma_{\text{bas./prism./pyr.}}}{\sum_{\alpha=1}^{N_s} |\gamma_\alpha|}, \tag{27}$$

where $\Gamma_{\text{bas./prism./pyr.}} = \sum_\alpha |\gamma_\alpha|$ represents the sum of either all basal, all prismatic, or all pyramidal slip activity. We define an analogous *relative TT activity*

$$\mathcal{Y}_{\text{TT}} = \sum_{\beta=1}^{N_t} \lambda_\beta, \tag{28}$$

which is a qualitative measure of the overall TT activity ($\mathcal{Y}_{\text{TT}} = 0$ implying no TT activity). Let us comment on the individual load cases and their predicted microstructural characteristics.

c-axis compression:

Mg crystals under plane-strain compression along the c-axis of the crystal are distinguished by strong strain hardening, characteristically followed by rapid fracture at roughly 4% to 6% strain (Kelley and Hosford, 1967; Wonsiewicz and Backofen, 1967). The resulting limited formability is related to the localization of deformation due to an insufficient number of deformation modes, resulting in the formation of shear bands and ultimately failure (Nie et al., 2020; Sandlöbes et al., 2011; Wonsiewicz and Backofen, 1967; Kelley and Hosford, 1967). Both cases A and B are similar in nature, B showing a slightly higher peak stress (Wonsiewicz and Backofen, 1967; Kelley and Hosford, 1967). The reduced model captures this phenomenon accurately.

The relative activities in Fig. 7 for cases A and B show a predominant activation of pyramidal systems, which agrees with the results by Zhang and Joshi (2012), Wang et al. (2019). In the absence of CTs, pyramidal slip is the only option to accommodate compressive c-axis deformation. Experimentally, the presence of pyramidal slip at room temperature was shown by Obara et al.
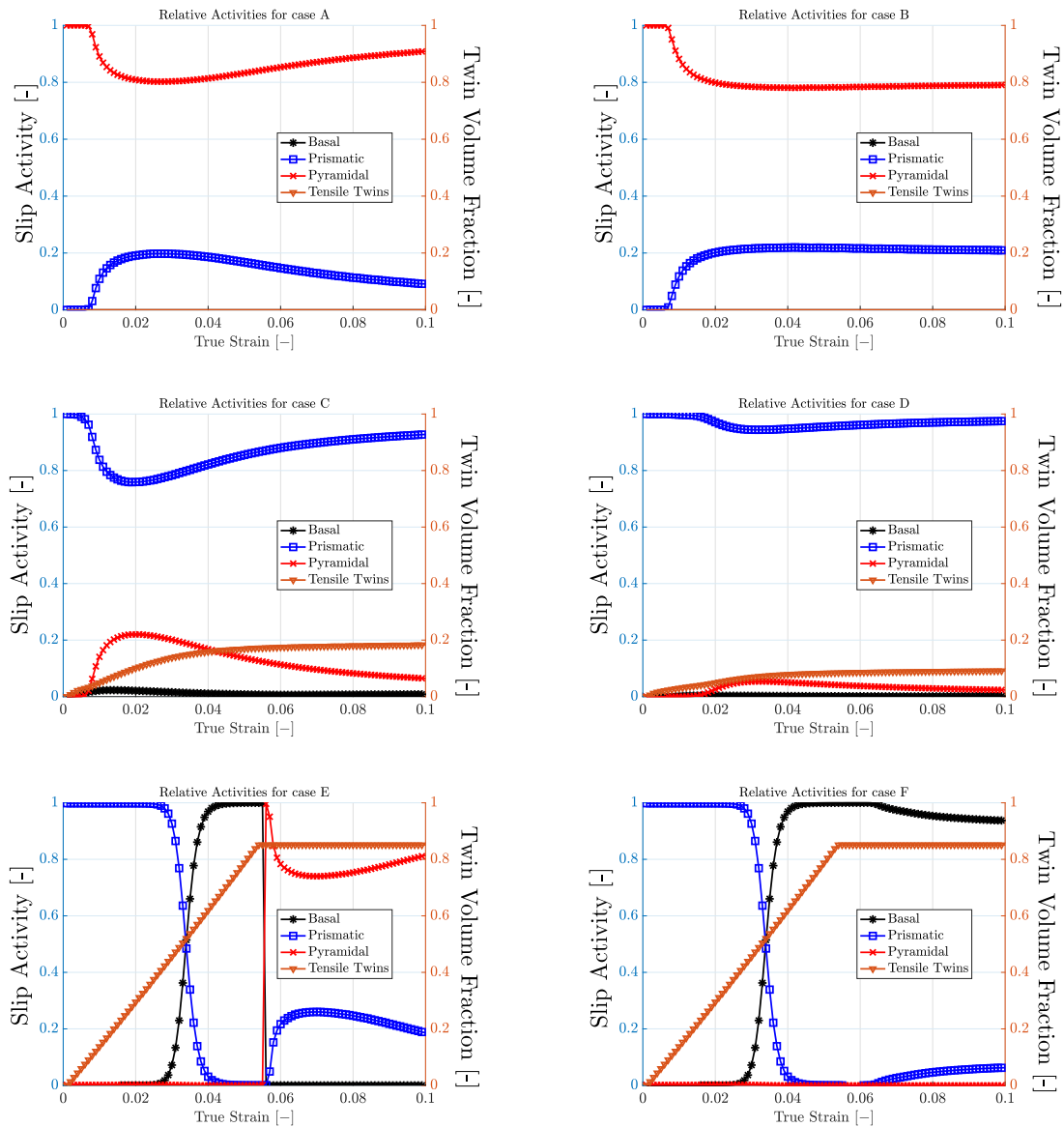
Fig. 7. Relative twin and slip activities for cases A, B, C, D, E, and F. Case G shows only basal activity, as expected, and is hence omitted here.

(1973), Muránsky et al. (2008), Ono et al. (2004), Lilleodden (2010). Since the pyramidal II systems have a Burgers vector with both, *c*- and *a*-components, and a constraint is applied, some of the deformation along the *a*-axis induced by the activity of the pyramidal systems requires compensation. This induces a smaller degree of prismatic slip. The change in orientation in case B leads to an increased activity in the prismatic systems. Similar effects were reported in previous numerical studies (Zhang and Joshi, 2012; Chang and Kochmann, 2015; Liu et al., 2017). The larger peak strain in case B comes from the effect of the constraint which effectively hardens the pyramidal systems (Zhang and Joshi, 2012) as well as the increased slip activity on the prismatic systems, which lead to a hardening effect.

a-**axis compression with constrained** *c*-**axis:**

Mg single-crystals under *a*-axis compression typically exhibit strong initial strain hardening, followed by a gradual strain softening and no explicit peak stress. This case is also characterized by an exceptionally high ductility, as it can accommodate large strains before fracture (Kelley and Hosford, 1967; Wonsiewicz and Backofen, 1967). This behavior is accurately described by the present formulation. In both cases C and D, the constraint is applied in the {0001} direction, and the prismatic systems are expected to be the predominant sources of plastic slip. In addition, the non-zero resolved stresses on the TT systems along with their low CRSS lead to a significant amount of TTs despite the hard constraint. The deformation along the *c*-axis, which results from the TTs, is offset
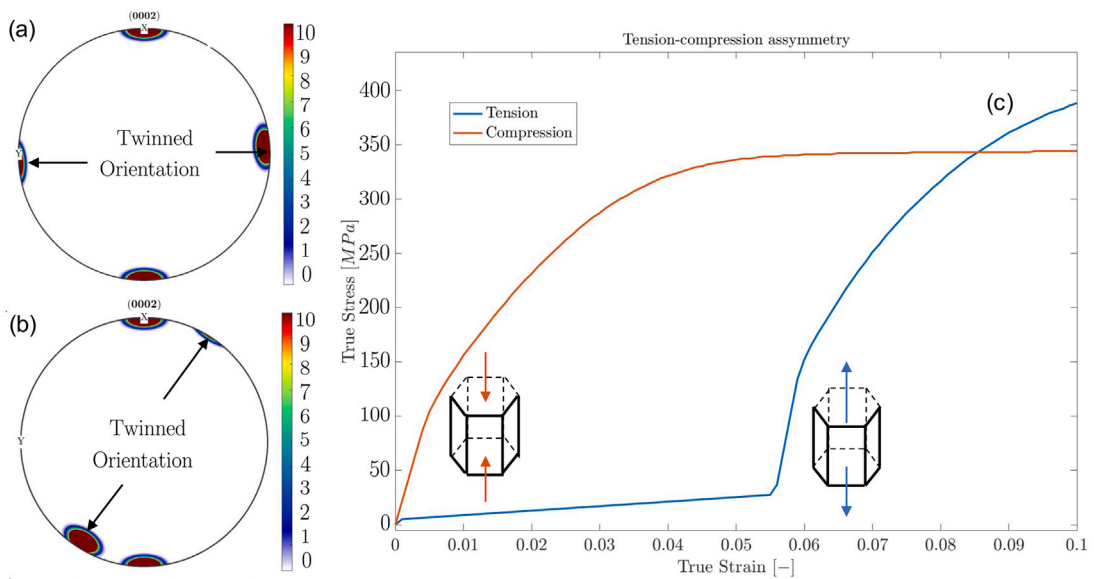
Fig. 8. Tension–compression asymmetry and the reorientation of the crystal: due to the imposed initial orientation of the crystal, the *x*-direction is unconstrained, and the loading direction corresponds to the *y*-direction in the pole figures (a.b). Case E leads to a reorientation by 86° (a), whereas case F leads to a reorientation by 30.3° (b) (Wang et al., 2019; Wonsiewicz and Backofen, 1967). (c) shows the tension–compression asymmetry of the TT system, which is active under *c*-axis extension but inactive under *c*-axis compression.

by elastic deformation in the channel wall as well as by the activity of CTs in an experimental setting, allowing up to 20% twin volume fraction (Wonsiewicz and Backofen, 1967). In our simulations, however, the channel is rigid and CTs are not accounted for in the reduced model, yet TTs are also observed. This is possible as the strain along the constrained *c*-axis due to TTs is offset by activating the pyramidal systems. Case C exhibits a larger TT contribution, which plateaus at about 3% strain. In agreement, the pyramidal II contributions tend to vanish beyond this level of strain, as little *c*-axis deformation is induced (see Fig. 7). Conversely, case D exhibits less TT activity, in agreement with the pyramidal activity also being reduced.

a-axis compression with unconstrained c-axis:

Cases E and F are dominated by TTs, characterized by low strain hardening up to 6% strain. TT in Mg is easy to activate, and twins grow until they reach saturation, thus showing little strain hardening during the initial deformation phase (see Fig. 6). Upon saturation, the crystal reorients abound the twin plane of the active twin system, which leads to a drastic change in the stress–strain response, as demonstrated by cases E and F.

Twinning is an asymmetric deformation mode,[2] which is captured by the reduced model, as shown in Fig. 8.

For case E, the unobstructed *c*-axis allows the TT to grow, contributing a $\langle c+a \rangle$ component to the total deformation. Initially, this leads to the activation of prismatic systems to offset the $\langle a \rangle$ contributions against the constraint. After about 2% strain the crystal has sufficiently reorientated due to slip, so that basal slip becomes active and almost instantaneously governs the deformation. The twin system saturates at about 6%, which leads to an instantaneous change in the stress–strain behavior. In case E of the simulations, the twins reorient the material by 86.3°, which is close to the orientation initially shown in cases A and B (Kelley and Hosford, 1967). In this configuration, the shear stress on the basal systems is minute, in contrast to the pyramidal systems, which are now again favorably aligned. Note also that the total amount of slip is small during the first 6% of deformation, since the pyramidal slip almost instantaneously accounts for the majority of all slip upon reorientation. The reoriented crystal is close to cases A and B, but the response is stiffer, which was also noted by Kelley and Hosford (1967) and which is attributed to prior twin-hardening of the material.

The situation is different for case F, where the twins reorient the material such that the basal plane forms a 31° angle with the loading direction (Fig. 8), thus enabling basal slip to emerge easily (Kelley and Hosford, 1967). As noted by Wang et al. (2019), the orientation of case F leaves the basal systems ideally oriented and explaining the different behavior of the twinned crystal. Further, in case F four TT systems are ideally oriented for activation, as noted by Kelley and Hosford (1967). As seen in Fig. 8, we capture the reorientation of both cases E and F accurately in our simulations. The discrepancy in the predicted stress for case F is due to other aspects. The predominant twin model used here (only the twin system with the largest CRSS is active) cannot capture multiple

---

[2] The characterization as a "*compressive*" vs. "*tension*" twin depends on the c/a ratio of the material (Yoo, 1981). For materials with a $c/a < \sqrt{3}$ (which includes Mg) the $\{10\bar{1}2\}$ twinning mode is a tension twin, i.e., it elongates the *c*-axis. It hence activates under *c*-axis tension, while showing no activity under *c*-axis compression.
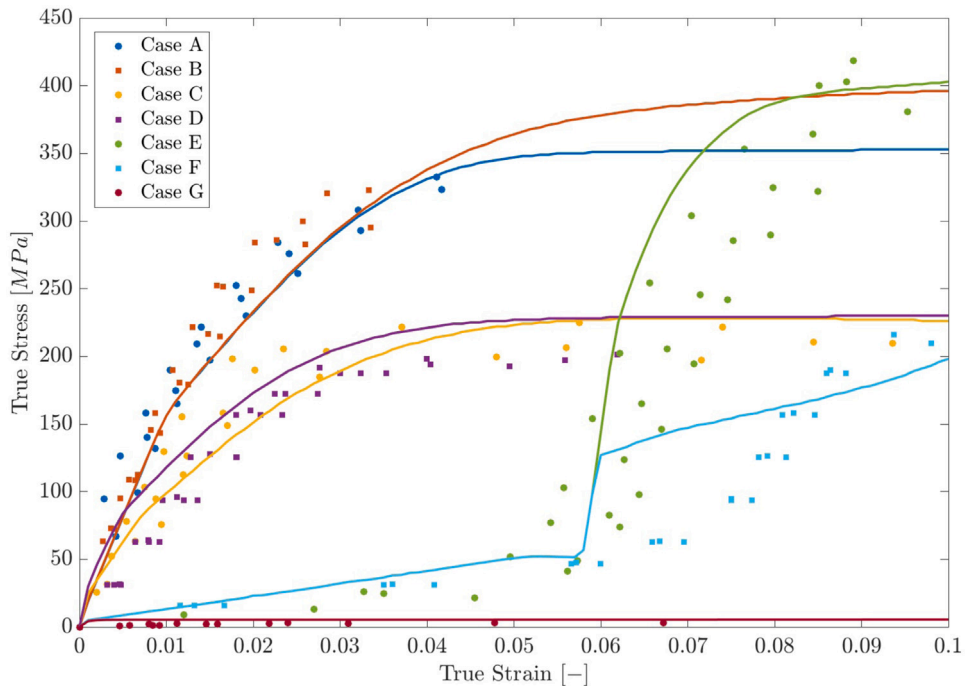
Fig. 9. Stress–strain responses of cases A through G, as obtained from the full model including CT. Dots represent experimental data of Kelley and Hosford (1967), lines are simulated results.

twin systems. This leads to premature saturation of a single system and the subsequent lack of twin-slip hardening yields a lower stress at larger strains.

Orientations promoting basal slip:

Under plane-strain compression with the *c*-axis forming a 45° angle to the compression direction (case G), basal slip is favored. Samples in this case exhibit considerably higher plastic strains and noticeable hardening is observed only at large strains, as is evident from the data of Kelley and Hosford (1967), Nie et al. (2020). The low hardening rates and early onset of plasticity reflect the discrepancy in CRSS and hardening behavior between the basal systems and all others, as basal slip is solely active up to 10% strain in this case. At higher strains, deformation is also accommodated via twin band formation. After about 50%–60% strain, the crystal hardens extensively, as the twinned volume fraction increases (Nie et al., 2020).

4.1.2. Full representation (including CT)

The full model including CT (calibrated through cases A and C, as explained in Section 3) leads to the stress–strain responses shown in Fig. 9 for all seven cases. Again, good agreement with experiments is achieved, and the key aspects of the stress–strain behavior are captured. CTs lead to a slightly stiffer initial response for cases A and B as well as under reorientation due to twinning. This is related to the high hardening and slow kinematics of the twin propagation generally associated with CT (Zhang and Joshi, 2012; Wonsiewicz and Backofen, 1967; Wang et al., 2019) as well as with the change in CRSS and initial hardening parameters of the pyramidal systems, as obtained from the calibration of the full model (see Table 2). Predictions for cases E, F, and G are close to those of the reduced model, so that we will focus on the cases A and C to discuss the influence of CTs.

c-axis compression:

CTs offer a second deformation mode next to the pyramidal II systems to accommodate deformation along the c-axis under compression, while also affecting the crystal reorientation. Fig. 10 shows the activity of the deformation modes, highlighting the competition between the CT and pyramidal II systems. Initially, basal slip occurs alongside CT formation in agreement with experimental observations (Wonsiewicz and Backofen, 1967). The reorientation due to CT is, however, minimal, seen over the entirety of the crystal, and the volume fraction remains below 10% for the duration of the simulation. CTs are known to propagate more slowly than their tensile counterparts (Zhang and Joshi, 2012) and to harden more extensively. Due to the slow propagation of CT lamellae in the crystal (described in our model by the reduced reference growth rate) the crystal must activate pyramidal slip once the CT systems have hardened substantially (which occurs at about 3% strain, when the CT system has hardened so much that any further increase in the twin volume fraction is unfavorable). The deformation is henceforth accommodated by a combination of pyramidal and prismatic slip, in a similar fashion to case A in the reduced configuration.
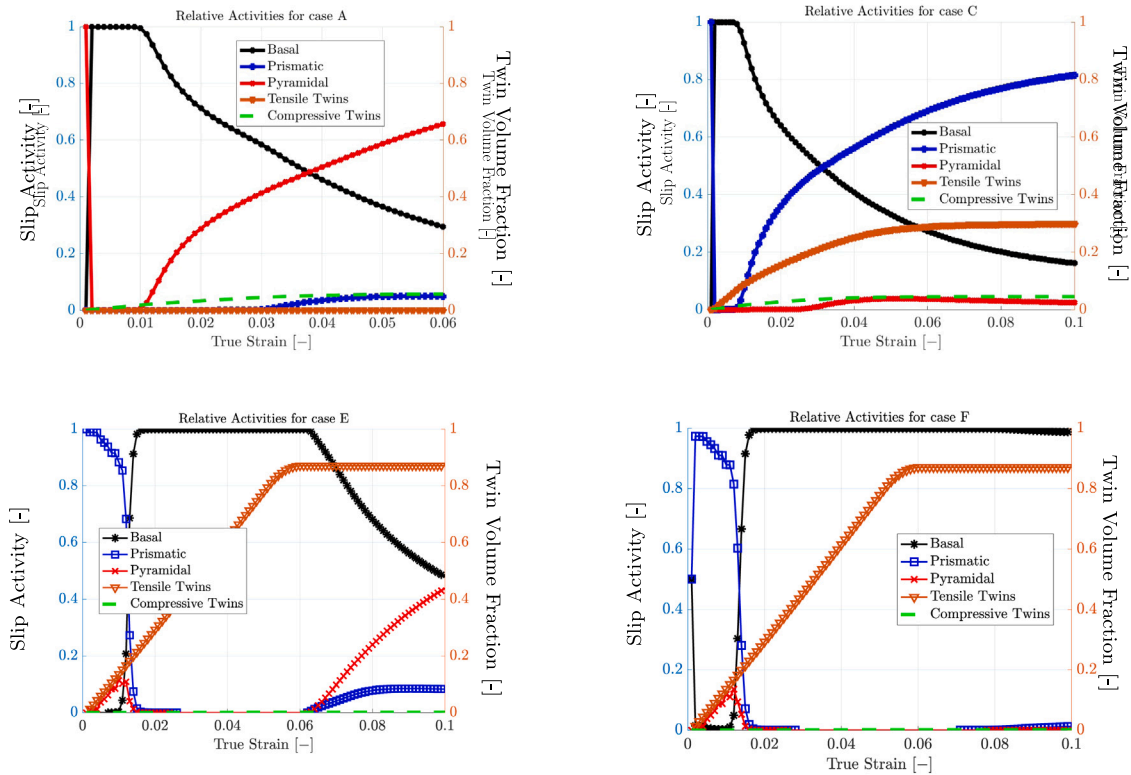
Fig. 10. Relative activities of the deformation modes, as obtained from the full model including CT. Results are for a single-crystal under plane-strain compression, mimicking cases A, C, E, and F of the experiments by Kelley and Hosford (1967).

a-axis compression with constrained c-axis:

Wonsiewicz and Backofen (1967) reported a significant amount of $\{10\bar{1}2\}$ twin formation with some $\{10\bar{1}1\}$ CTs, which "could only have happened to relieve the c-axis expansion generated by the $\{10\bar{1}2\}$ twinning". The CT banding is hence activated as a mechanism to reduce the stress induced by the TT formation. The full model captures this behavior, as shown in the relative activities in Fig. 10. Initially, a combination of basal slip, CT, and TT is activated, followed by a sharp increase in prismatic slip activity. Up to approximately 3% strain, CT balance the c-axis extension induced by TT. Upon hardening at strains larger than 3%, the CTs saturate and small amounts of pyramidal slip activity accommodate further c-axis deformation. TTs slowly saturate around 6% strain, which also leads to a reduction in pyramidal activity. a-axis deformation is accommodated by a combination of mostly prismatic and a smaller portion of basal slip.

a-axis compression with unconstrained c-axis:

Simulations of crystals with an unconstrained c-axis, again, show the typical twin-dominated deformation behavior, as seen with the *reduced* model. The initial deformation is accommodated mostly by the TT system alongside basal and small amounts of prismatic slip for compatibility reasons. At close to 6% strain, the twins saturate and the crystal is fully reoriented (Kelley and Hosford, 1967), bringing it close to the orientation of cases A and B. Upon reorientation in case E, pyramidal II slip is slowly activated in the reoriented region. Due to the larger CRSS of the pyramidal slip, the activity of this deformation mode increases more slowly than for the *reduced* model. Case F shows generally a similar behavior: the first 6% strain are governed by the TT system. Upon reorientation, however, due to the different orientation of the twinned region, the basal plane is favorably oriented for slip (Kelley and Hosford, 1967). Hence, basal activity is the key contributor to deformation in the reoriented crystal, which is captured accurately in both implementations of the model. The observed microstructures are generally in good agreement with the observations of Kelley and Hosford (1967) observations. One exception is the fact that Kelley and Hosford (1967) reported $\{10\bar{1}1\}$ activity right before fracture for case E, which is not captured here as we do not account for double-twinning.

4.1.3. Summary

In summary, both full and reduced models capture the stress–strain behavior of Mg qualitatively and quantitatively well in comparison to experimental data, which also extends to the microstructural mechanisms. The key difference lies in how deformation along the c-axis in compression is accommodated—either involving the CT systems or non-basal slip systems. Results indicate that
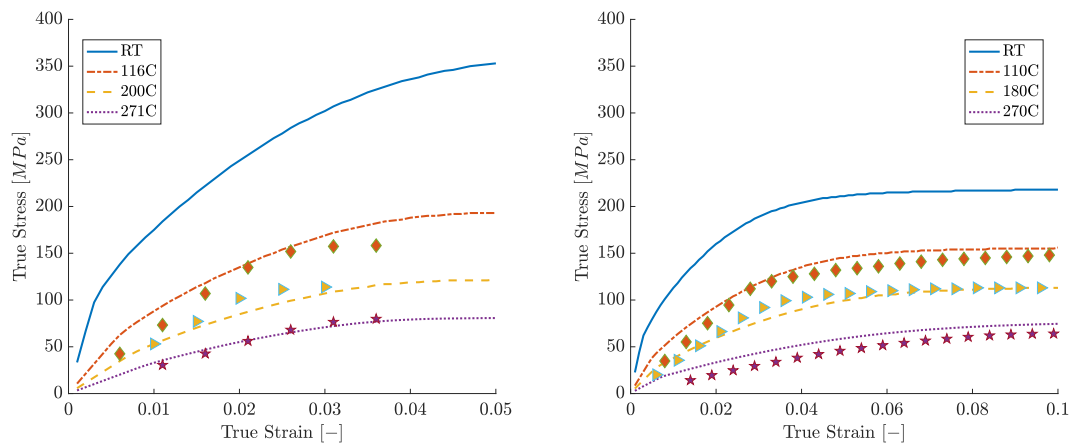
Fig. 11. Temperature-dependent stress–strain response of Mg single-crystals, corresponding to cases A (left) and C (right). Solid lines are predictions by the *reduced* model, whereas the scatter plot represents the experimental data obtained by Wonsiewicz and Backofen (1967).

both versions (with properly calibrated plastic material parameters, which differ in the full and reduced models) capture the salient stress–strain response. The full model, which includes the CT systems, shows the competition between the CT and the pyramidal systems, previously reported in experiments, and offers an insight into their relative activities at room temperature.

4.2. Temperature dependence of single-crystal Mg

Let us proceed to test the two models for their temperature-dependent predictions. While the basal and twin systems were chosen to be temperature-independent, prismatic and pyramidal slip undergo a strong increase in activity at elevated temperature (Ono et al., 2004; Chapuis and Driver, 2011; Nie et al., 2020). This has a marked influence on the activity of deformation modes with increasing temperature, as we will demonstrate in our comparison of results, again beginning with the reduced model before advancing to the full one.

4.2.1. Temperature dependence of the reduced model

As cases A and C prominently activate the temperature-dependent deformation modes, we evaluate these two cases for their temperature-dependent response. Experimental single-crystal data is available from Wonsiewicz and Backofen (1967) at temperatures of 116, 200, and 271 °C for case A, and at 110, 180, and 270 °C for case C. Fig. 11 shows good agreement between the model predictions and the experimental data under c-axis compression at four selected temperatures (results at 25 °C (room temperature, RT) are identical to those in Fig. 6). Strain hardening and peak stresses significantly reduce with increasing temperature, as expected. Differences at low strains primarily stem from the fact that, as discussed before, the experimental data of Kelley and Hosford (1967) and Wonsiewicz and Backofen (1967) differ (hardening rates in Wonsiewicz and Backofen (1967) are consistently smaller than those of Kelley and Hosford (1967), while the peak stresses match closely). Since we calibrated the single-crystal RT response with the data of Kelley and Hosford (1967), the observed differences especially in the low-strain regime may be expected. In fact, such strong temperature-induced softening in the experimental data in the low-strain regime seems unusual. Other data from Ono et al. (2004), Chapuis and Driver (2011) do not show such behavior; however, Ono et al. (2004) provide only polycrystal data, while Chapuis and Driver (2011) does not provide sufficient data at elevated temperature. Further, note that above 170 °C the material is prone to show crack formation as noted by Wonsiewicz and Backofen (1967). As we do not capture failure in this model, an overestimation of the stresses at large strains is the result. Dynamic recrystallization (DRX) may also play a role (Wonsiewicz and Backofen (1967) reported that twinned regions often show recrystallized areas, even at room temperature; Sitdikov and Kaibyshev (2001) noted low-temperature twin DRX as a mechanism in Mg, alongside the early onset continuous and discontinuous DRX depending on the temperature). While such effects are not accounted for in the chosen SCP model, the overall temperature-dependent stress–strain behavior at all shown temperatures is captured adequately. This includes the typical reduction in yield stress and work hardening with increasing temperature.

Kang et al. (2012) reported that pyramidal slip may be tightly related to dynamic recovery mechanisms in Mg. As the dislocations move across dislocation lines by double-cross slip, they lead to dislocation annihilation. This increases the ductility of the material and reduces work-hardening. While the present SCP model does not capture recovery, the chosen temperature-dependent formulation reproduces the reduced work hardening with increasing temperature due the strong decrease of the self- and crosshardening parameters.

In case C, the crystals are oriented with their c-axis perpendicular to the loading direction and hence show higher ductility. The model accurately predicts the stress–strain response of this case throughout the temperature range (see Fig. 11). Again, experimental data show discrepancies, yet predictions deviate less from experiments than in case A. The low hardening rates reported in experiments (and seen in Fig. 11) are captured by the strongly reduced self-hardening factors. Overall, the reduced model reflects the experimentally observed single-crystal response of Mg properly.
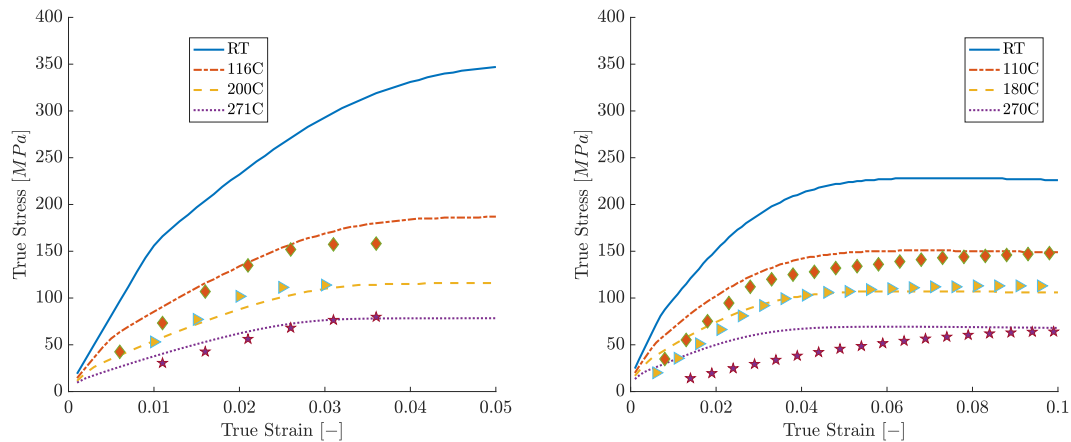
Fig. 12. Temperature dependent stress–strain response of Mg single-crystals, corresponding to cases A (left) and C (right). Solid lines are predictions by the *full* model, whereas the scatter plot represents the experimental data of Wonsiewicz and Backofen (1967).

4.2.2. Temperature dependence of the full model

It is often assumed that CTs show a strong temperature dependence and are either more active (Wang et al., 2019) or less active (Barnett, 2007) at elevated temperature. The reduced activation barrier for pyramidal slip at elevated temperature leads to the preferred activation of this slip mode over CT. Barnett (2007), Barnett et al. (2008), Liu et al. (2017) reported temperature dependence in the activity of twinning, notably the existence of a transition temperature for Mg and Mg alloys (around 450–475K in pure Mg, which is affected by alloying elements), above which CT activity is reduced at the expense of other deformation modes, contradictory to the observations made by Wonsiewicz and Backofen (1967), who observed an increase in CT activity under c-axis compression at all tested temperatures. The stress–strain curves for cases A and C are shown in Fig. 12. Surprisingly, the single-crystal curves obtained by Wonsiewicz and Backofen (1967) show relatively strong softening in the initial region, which is in disagreement with temperature data from Chapuis and Driver (2011) and polycrystal data from Ono et al. (2004).

With the full model, good agreement with experiments is obtained for the individual cases, except for case C at the highest temperature, where the initial hardening rates are overpredicted significantly. This may be attributed to the early onset of recrystallization in experiments (Wonsiewicz and Backofen (1967) noted the presence of recrystallization, especially in twin bands), which is not captured by the model.

To highlight the predicted microstructure evolution, Fig. 13 shows the slip activities for case A at 271°C. For both models, the contribution of pyramidal slip increases with increasing temperature, indicating that the pyramidal systems tend to dominate the competition with CTs. The model agrees with the experimental observations of Barnett (2007) and Khosravani et al. (2013), who observed increased pyramidal activity. The reduced hardening also allows for higher levels of deformation to be accommodated by this deformation mode alone (compared to at room temperature). Nevertheless, CTs remain present in the full model (they may vanish at higher temperature, but this outside our scope).

In both models prismatic slip dominates the deformation during case C at elevated temperature with only minor differences. In the reduced model, we attribute the predicted presence of pyramidal slip to the constrained $c-$direction, while TTs also contribute to the deformation at elevated temperature—in agreement with experimental observations by Wonsiewicz and Backofen (1967). However, TT is reduced to lower volume fractions than at room temperature. The full model shows a similar transition in deformation modes, with more slip activity on the prismatic systems and TT. Unlike at room temperature though, the pyramidal systems seem to be activated to offset the TT-induced elongation of the c-axis.

In conclusion, the full model captures the competition between the CT and pyramidal systems accurately across the examined range of temperatures, and a good correlation with the experimentally reported microstructural deformation modes is observed. In all cases, the CT volume fraction remains small despite the included temperature dependence of their CRSS values and hardening parameters in the model. This hints at the fact that the CT systems may in fact not be temperature-dependent (the inclusion of temperature dependence in the model has no impact on the predicted deformation modes), but that their apparent temperature dependence in experiments is implicitly a result of the temperature-dependent pyramidal systems.

5. Polycrystal simulations

Having calibrated the (full and reduced) models based on their single-crystal behavior, we now predict the temperature-dependent polycrystalline response at elevated temperature as a further means of validation in comparison with experiments (Wonsiewicz and Backofen, 1967).
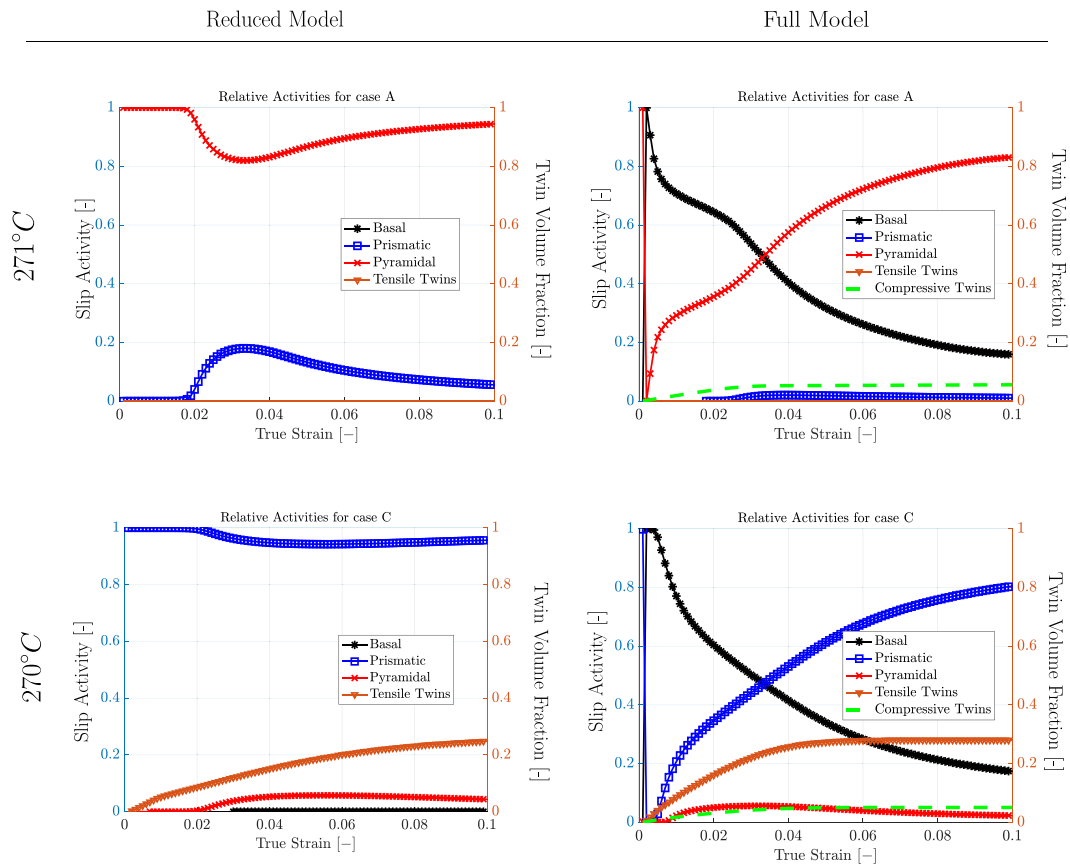
Fig. 13. Relative activities of the slip and twin systems in Mg single-crystals for cases A at $271°C$ and C at $270°C$. Results on the left were obtained from the reduced model, results on the right from the full model.

5.1. Convergence of the Taylor model

We first verify that the chosen Taylor model converges with increasing number of grains. We perform a set of 20 simulations with 24 to 200 grains, whose average stress–strain responses are shown in Fig. 14 (in comparison with experimental results from Kelley and Hosford (1967)). The corresponding texture for the polycrystal simulations is shown in Fig. 15.

Initially, the grains show a purely elastic response, hence the close agreement of all curves at strains $\epsilon < 0.03$. For 24 and 50 grains, we observe a large spread in the stress–strain response, as individual grains can have a significant impact on the average response. For 200 grains both convergence and a good approximation of the experimentally measured response are observed. We therefore deem a total of 200 grains sufficient and perform all following polycrystalline simulations with 200 grains, unless otherwise indicated.

5.2. Textured polycrystals at room temperature

Next, we perform channel-die simulations of textured polycrystals at room temperature. At room temperature, we simulate the cases labeled ZT, RT, and ZR among the experiments of Kelley and Hosford (1967). All grains are assumed to have identical volume fractions and initial orientations chosen to qualitatively match the pole figures reported by Kelley and Hosford (1967), as shown in Fig. 15. Fig. 15 confirms that the reduced model captures the stress–strain response of the textured polycrystals quantitatively well, with small deviations attributed to variations in the texture, experimental uncertainties, and the Taylor model's tendency to over-predict stresses.

In case ZT, most grains have their c-axes oriented along the loading direction, while being constrained in the transverse direction. The stress–strain response resembles strongly that of single-crystal cases A and B (Fig. 6), yet with lower peak stresses. This is due to the non-ideal orientation of the crystals compared to cases A and B, so that basal slip is favored in many grains (Kelley and Hosford, 1967)—especially in the Taylor model, grains with lower peak stresses reduce the average response.

Case RT represents compression along the rolling direction with a constrained transverse direction, so that the c-axis of the majority of grains is allowed to extend. This configuration promotes significant amounts of twinning, whose reorientation of grains
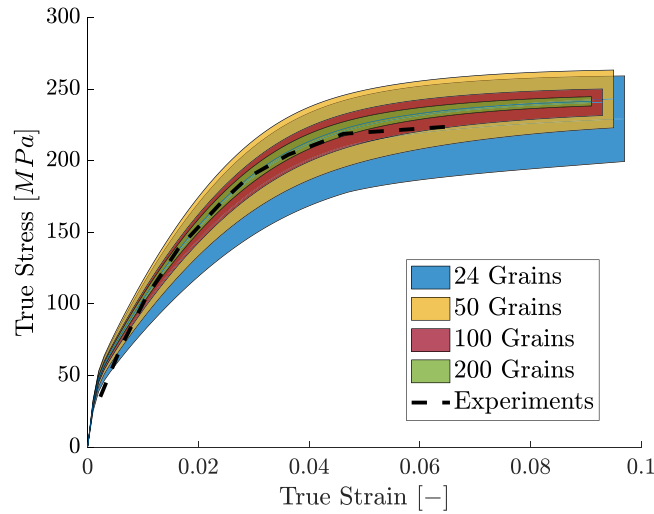
Fig. 14. True stress–true strain response of textured polycrystals of pure Mg from experiments (dashed line) and from simulations with 24, 50, 100, and 200 grains simulated with the reduced model. Experimental data are from Kelley and Hosford (1967).
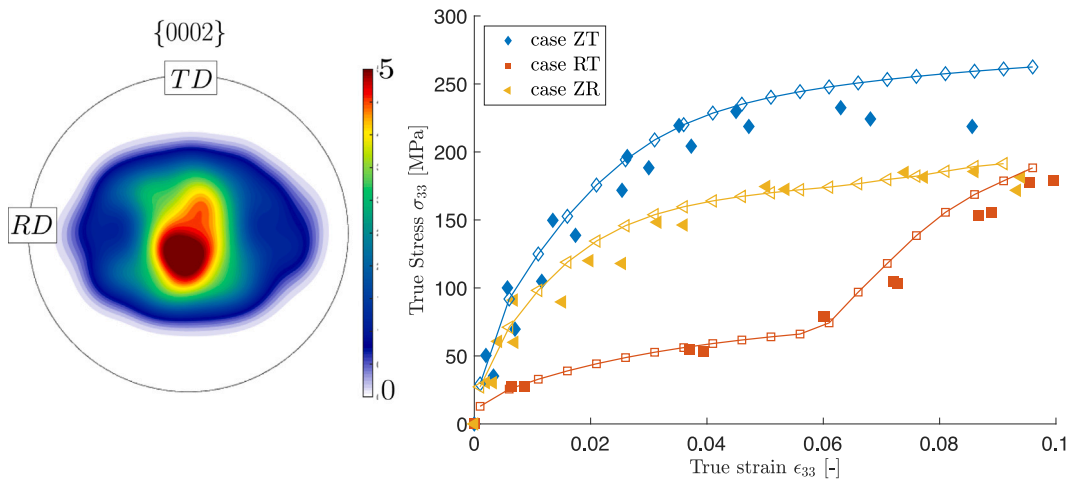

Fig. 15. True stress vs. true strain response of textured polycrystals of pure Mg from experiments (markers) and from simulations with the reduced model (solid lines) at room temperature. The experimental data was obtained by Kelley and Hosford (1967). The *representative* texture utilized for the simulations is shown on the left and was chosen such as to approximate the texture reported by Kelley and Hosford (1967).

leads to a stiffened response at approximately 6%, analogous to single-cyrstal cases E and F. The transition in the homogenized polycrystal case is less sharp than for single-crystals, as may be expected. Finally, case RZ imposes compression in the rolling direction with a constrained normal direction, i.e., the *c*-axis extension of the majority of the grains is constrained. The resulting stress–strain curve is close to single-crystal cases C and D. (The same observations were made by Kelley and Hosford (1967).) We conclude that the Taylor model captures the room-temperature response of textured polycrystals under different loading directions qualitatively and quantitatively well.

5.3. Temperature-dependent response of textured polycrystals

A comparison of simulation results with experimental polycrystal data at both room and elevated temperature is summarized in Fig. 16, using the experimental data of Wonsiewicz and Backofen (1967). These authors reported a texture that appears to be similar to Kelley and Hosford (1967) but less pronounced. As no precise texture information was provided, we chose – based on the descriptions in Wonsiewicz and Backofen (1967) – the one shown in Fig. 16. Wonsiewicz and Backofen (1967) described the texture in their experiments as follows: "Under metallographic examination with polarized light, the material was found to be textured, somewhat diffusely but with {0001} poles clustered around the sheet normal and spreading outwards by as much as 50°". We obtain the texture in Fig. 16 by assuming a normal distribution of the {0001} poles around the normal direction with a standard deviation
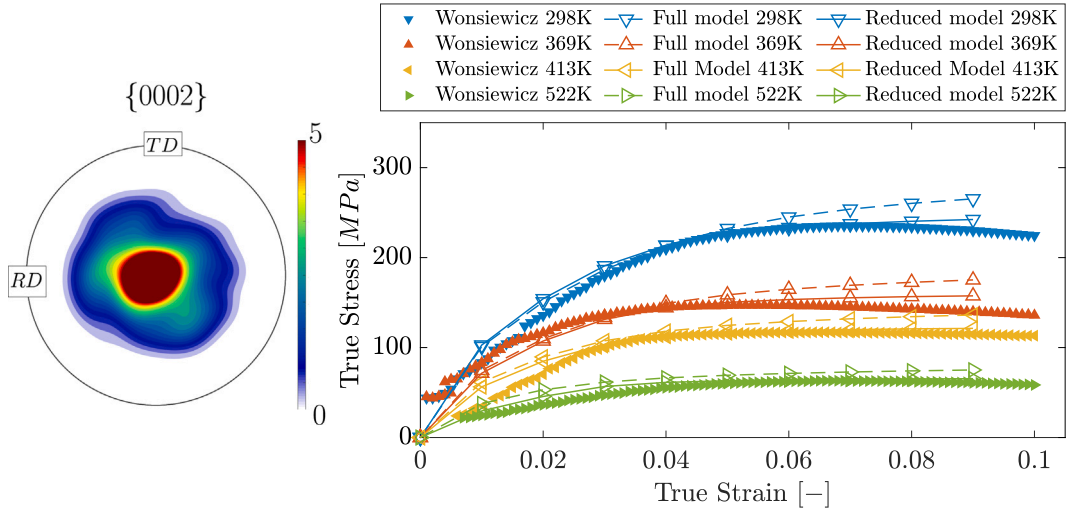
Fig. 16. True stress–true strain response as obtained from polycrystal simulations, using the full and reduced models. Markers correspond to experimental data from (Wonsiewicz and Backofen, 1967), solid lines show the response predicted by the reduced model, dotted lines by the full model. The shown texture (used in simulations) was obtained by assuming a normal distribution with expectation value at the basal pole and outliers as far as 50° from the normal direction.

of 25°. Compression is applied along the normal direction (ND). The predicted stress–strain response of both (full and reduced) models agrees well with experiments.

Most grains in this case are aligned with the ND (and hence similarly as in single-crystal cases A and B). The polycrystal exhibits relatively strong initial hardening in the plastic regime around 1%–3% strain, before the stress gradually plateaus. In comparison to the single-crystals, the stress reaches its peak more gradually and the peak stresses are reduced, which stems from the influence of all other grains oriented away from the ND and contributing to the polycrystal response. At 25 °C and 96 °C, crystals in experiments were observed to show crack formation (Wonsiewicz and Backofen, 1967) at 7%–10%, which explains the reduction of stresses at that level of strain as compared to simulations (which do not model material failure).

Both models capture the incipient behavior up to 5% strain accurately, including the temperature-induced softening. At larger strains, experimental polycrystals showed cracks and strain localization (Wonsiewicz and Backofen, 1967; Kelley and Hosford, 1967). Further, effects such as grain boundary sliding may lead to softening. The Taylor model, agnostic to those effects, consequently over-estimates stresses in the large-strain regime. It is, however, noteworthy that the full model generally predicts a higher stress level than the reduced model. We attribute this to the presence of CTs, which in turn harden the TT systems (one of the weakest deformation modes). The accuracy improves with elevated temperature, providing further evidence for this assumption. As the pyramidal systems become more prevalent, the hardening linked to CT has a smaller impact.

5.4. Texture evolution

As a representative example, let us first study the texture evolution of a rolled sample of pure Mg under uniaxial compression along the rolling direction (RD). The initial texture of the polycrystal is chosen to mimic a typical rolled sheet of Mg, see Fig. 17, which shows a strong pole in the normal direction (ND).

Assuming volume-preserving deformation due to small elastic strains and plastic incompressibility, we apply the deformation gradient

$$\boldsymbol{F} = \begin{bmatrix} (\dot{\varepsilon}t)^{1/2} & 0 & 0 \\ 0 & (\dot{\varepsilon}t)^{1/2} & 0 \\ 0 & 0 & \dot{\varepsilon}t \end{bmatrix}$$

with strain rate $\dot{\varepsilon} > 0$ and t denoting time, to the polycrystal model up to a true strain of 20%. At room temperature, samples are expected to show cracks at larger strains, hence setting a limit to the applied deformation. The simulated texture before and after deformation is compared in Fig. 17. The initially strong basal pole in the ND transforms into a weaker pole in the transverse direction (TD), capturing the essential feature of texture reorientation due to twinning and slip and qualitatively in agreement with observations made for AZ31B (Jain and Agnew, 2007).

As a further example, we investigate the texture evolution during cold and hot asymmetric rolling. Rolling is assumed to be a superposition of compression and simple shear (Chang, 2016), so it can be simulated by applying the deformation gradient

$$\boldsymbol{F} = \begin{bmatrix} e^{\dot{\varepsilon}t} & 0 & \alpha \cdot \dot{\varepsilon}t \\ 0 & 1 & 0 \\ 0 & 0 & e^{-\dot{\varepsilon}t} \end{bmatrix}$$
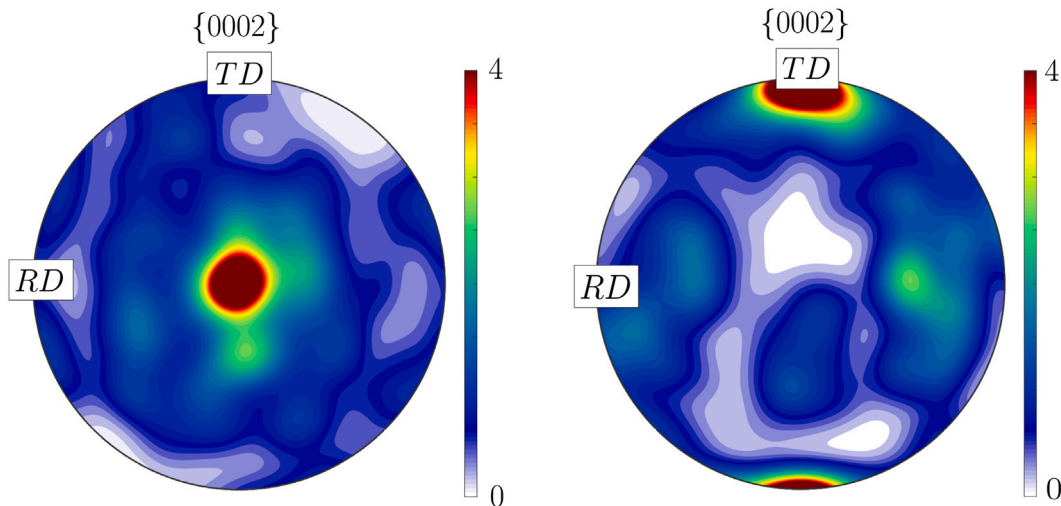
with a constant $\alpha = 3$.

Fig. 17. Texture of the undeformed (left) and deformed (right) polycrystal of pure Mg, simulated by the reduced model for the case of compression up to 30% true strain at 25 °C. Initially a strong pole in the normal direction exists (left). After deformation, most grains are reoriented due to twinning, leading to a new, weaker texture with the pole in the transversal direction (TD) (right).

We observe the formation of a split basal pole, which is slightly tilted towards the RD. The tilt is typical for the processing during asymmetric rolling, investigated here, and was reported similarly in experiments with commercially pure Mg by Beausir et al. (2009). As noted by Styczynski et al. (2004), the texture evolution obtained from including basal, prismatic and pyramidal II slip as well as TTs in the Taylor model leads to the formation of a fibrous texture; similar results were obtained by Chang and Kochmann (2015), Agnew et al. (2001) in their rolling simulations. Here, we investigate the impact of CTs on the texture development of a polycrystal with 1000 grains and an initially randomized texture, comparing the cold-rolled textures with and without CTs. For both full and reduced models, the formation of a fibrous texture is observed (see Fig. 18). Most grains adopt an orientation close to the basal pole but split either way of the TD (the vertical axis). Similar trends were observed during numerical studies (Chang and Kochmann, 2015; Styczynski et al., 2004; Agnew et al., 2001) and in a less pronounced manner for certain Mg alloys in experiments (Huang and Logé, 2016). This indicates that the pyramidal systems are highly active (Styczynski et al., 2004; Chang and Kochmann, 2015; Agnew et al., 2001). Additionally, Styczynski et al. (2004) discussed the influence of various deformation modes and reached the conclusion that the $\langle c + a \rangle$-pyramidal systems play a major role in the splitting of the poles. They noted that a splitting of the basal pole in $\pm 15°$ around the TD is commonly observed in AZ31, while Agnew et al. (2001) reported such a trend during processing of pure Mg. The same behavior has been observed for Mg-3Li alloys in the experiments of Agnew et al. (2001), further emphasizing the impact of precipitates and alloying elements on the texture evolution.

In their viscoplastic model, Agnew et al. (2001) found a similar behavior as Styczynski et al. (2004) for the evolution of Mg sheets during rolling, yet they were able to mitigate it by increasing the CRSS of the pyramidal systems to effect an increased activity of basal and prismatic $\langle a \rangle$ dislocations.

As observed in the previous sections, CT saturate due to self-hardening at relatively low strains. Therefore, during simulated rolling with an applied thickness reduction of up to 60%, the influence of the CT remains small. We therefore cannot observe a direct impact of the CT systems. Due to the early crack formation at low thickness reductions below 30% (Xin et al., 2011), cold-rolling of Mg is typically performed in multiple passes. Hence, for a better representation, the deformation during rolling must be applied incrementally, while accounting for thermal treatment in between passes, as is customary in industrial rolling processes. The present model cannot account for those factors. Further, in the case of a Taylor model, which is – adopting the wording of Styczynski et al. (2004) – a "compatibility first" model, the texture evolution is severely impacted by the constraint of uniform deformation across all grains. Better agreement with experimental textures may hence be found by relaxing this constraint through another homogenization approach.

6. Discussion

The presented full and reduced models (with and without CTs) have obvious differences and limitations, which we briefly discuss here. As the main difference, the single-crystal results highlighted the competition between the pyramidal II and the CT systems. Under c-axis compression, the reduced model can accommodate the deformation only via the activation of pyramidal slip, whereas the full model accommodated the early stages of plastic deformation via a combination of basal slip and CTs. Even though the effective stress–strain curves were similar, the underlying microstructural deformation modes differed substantially. In the full model, CTs were observed to saturate at relatively low strains, which is attributed to the slow kinetics of this system (Zhang and Joshi, 2012) as well as the strong self-hardening. With the saturation of CTs at low volume fractions, we infer that no viable deformation
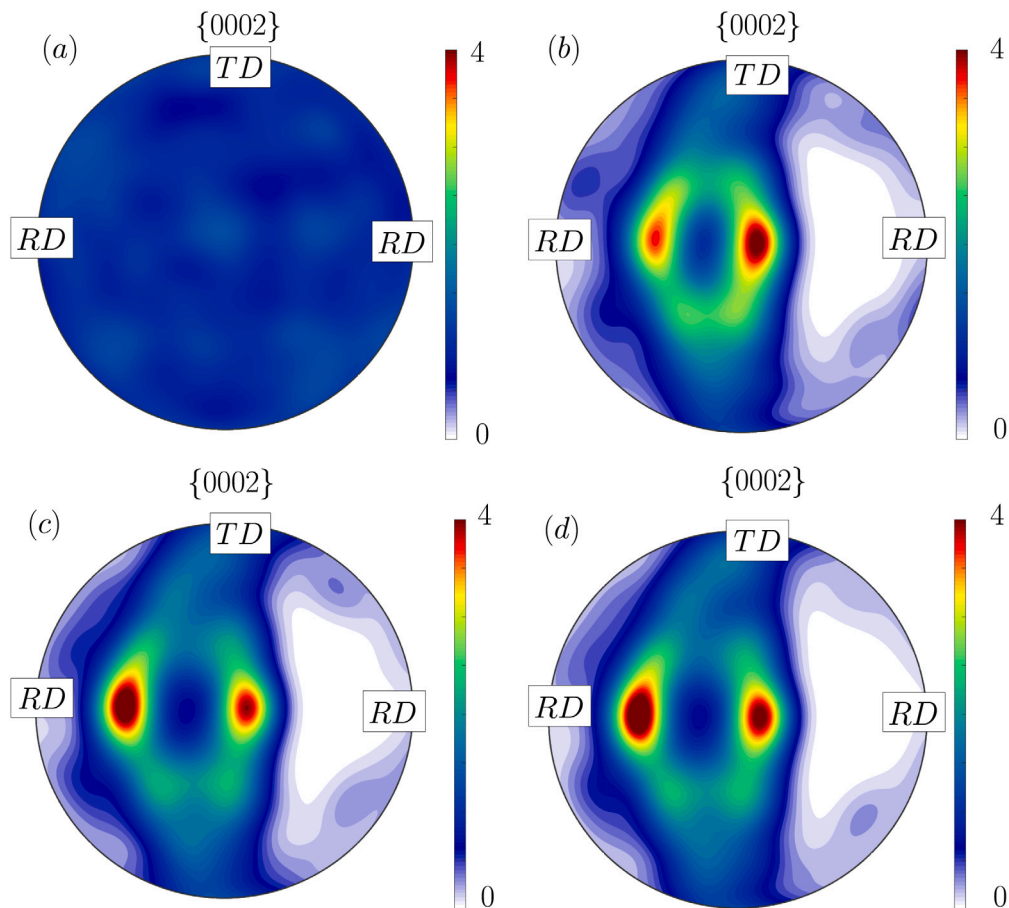
Fig. 18. Texture of a polycrystal of 1000 grains: (a) initial random grain orientations (b) cold-rolled texture simulated by the reduced model, (c) hot-rolled texture predicted by the full model including CT, and (d) hot-rolled texture predicted by the reduced model. The simulations were performed up to a total of 60% strain at a strain rate of $\dot{\epsilon}_{\text{true}} = 10^{-4}\text{s}^{-1}$ at a temperature of 25 °C for the cold case and 270 °C for the hot case.

modes are available, and while traces of pyramidal II slip may occur, the strong self- and cross hardening of this deformation mode as well as the pinning of $\langle c+a \rangle$ dislocations observed by Kang et al. (2012) is what leads to significant basal slip suddenly occurring in the reoriented CT bands alongside $\{10\bar{1}2\}$ double-twinning, as observed in experiments by Wonsiewicz and Backofen (1967). The model captures such a behavior in essence. However, due to the lack of a failure criterion and the absence of double-twinning in the model, not all of the intricate microstructure evolution was captured. At elevated temperature, for both single- and polycrystals the behavior changes (Wonsiewicz and Backofen, 1967; Barnett et al., 2008). The apparent temperature dependence of CTs and even of TTs (Jain and Agnew (2007)) inferred that less twins overall are present in the material at higher temperature can be explained by increased activity on the non-basal slip systems (Barnett et al., 2008). These observations suggest that CTs are a sub-optimal deformation mode, occurring in the absence of pyramidal II slip out of necessity to accommodate the flow criterion. In reverse, these findings also indicate that the activation of non-basal slip is what leads to the apparent temperature dependence of the CT systems and, further, could be the key to increasing the ductility of Mg.

Calibration of both models is challenging, even at the single-crystal level, since the influence of each model parameter cannot be isolated and various deformation modes show similar stress–strain characteristics. The full model with its competition of c-axis modes proved to be more difficult to calibrate. Better agreement with experiments seems possible with an improved twin model, where the saturation of CT lies near the point of fracture. In addition, the presented full model likely understates the importance of CT mode by activating only a single twin system at a time. Nevertheless, the present assumption leads to a very good approximation for the TT systems and is hence unlikely to have a significant adverse impact. The inclusion of CTs in the model yields an overall hardening effect, as seen in Fig. 16. This is due to the twin–twin hardening of CTs on the TT mode—one of the easier-to-active deformation mechanisms to accommodate plastic deformation. Despite the challenges linked to including the CT systems, they play an important role on the microstructure evolution and require to be present for an accurate depiction of the material behavior.

We note that for both models a high self- and cross hardening is necessary for the pyramidal systems to capture the strong strain hardening. This observation can in part explain the nature of the ambiguity in experimental reports. Pyramidal II slip is clearly the best-suited deformation mechanism to accommodate c-axis deformation, and hence it is not surprising that it should occur to some

degree even at low temperature, as suggested by experimental results (Ono et al., 2004; Kulekci, 2008). The strong self-hardening, as well as the immobilization of $\langle c+a \rangle$-dislocations noted by Kang et al. (2012), however explain the scarcity of pyramidal II slip in some experimental observations. Further evidence for this hypothesis is found in observations by Lilleodden (2010). Increasing the temperature leads to a higher activity of the pyramidal systems and thus to strain softening and an increase in ductility Chakkedath et al. (2018). Seeing that pyramidal slip provides a large number of possible deformation modes (Sebastian et al., 2000; Kang et al., 2012) and considering the observations of Barnett (2007), Barnett et al. (2008), Obara et al. (1973), pyramidal slip must be the dominant mode at elevated temperature.

Model limitations lie in the simplified representation of the twins, which has implications on the accuracy of the twin predictions, as well as considering only the $\{10\bar{1}1\}$ CT variant. Further, the isostrain assumption for the Taylor polycrystal model is a strong approximation, which overpredicts local strains. While good agreement in the stress–strain data was observed, the texture evolution during rolling was not fully as expected in Mg (yet, this also depends on the chosen initial texture chosen for simulations). Further, the model does not capture (dynamic) recrystallization (DRX), whose nature in Mg is still not fully understood; see, e.g., Kecskes et al. (2021), Sitdikov and Kaibyshev (2001), Kaibyshev (2012) and references therein. Sitdikov and Kaibyshev (2001), Kaibyshev (2012) argued that Mg exhibits multiple forms of DRX, beginning with twin DRX at lower temperature, followed by a mixture of continuous and discontinuous DRX at higher temperature. For the present models, these factors cannot be accounted for, and, as already noted by Wonsiewicz and Backofen (1967), we have little understanding of their impact on the crystal behavior. There is, however, no doubt that at temperatures above 250 °C recrystallization plays an important role, setting a natural upper limit to the present model and calling for models including DRX (Tutcuoglu et al., 2019b,a; Walde and Riedel, 2007).

7. Conclusion

We presented a comparative study of two versions of a newly introduced temperature-dependent crystal-plasticity model for pure Mg, whose performance was demonstrated both on single- and polycrystals. Both versions of the model were calibrated based on single-crystal stress–strain data at room temperature and at elevated temperature. Validation was achieved via polycrystal simulations, which showed good quantitative agreement with experimental stress–strain data and qualitative agreement with experimental texture observations. Compared to spatially resolved plasticity models (Zhang and Joshi, 2012; Liu et al., 2017), the chosen Taylor-type crystal plasticity models showed similar behavior of the various slip and twin systems, confirming that the presented models capture the salient features of plasticity in Mg in an efficient setting. The following summarizes our findings:

- The new framework presented here describes the temperature-dependent response of pure Mg by accounting for the temperature dependence of the CT and non-basal slip systems at the single-crystal level. A comparative study of the full and reduced models (with and without CT) captured quantitatively the *temperature-dependent* stress–strain response and qualitatively the slip and twin activity observed experimentally in pure Mg single-crystals.
- The comparison of the two models highlights the competition of the CT and pyramidal II slip systems in pure Mg. Results indicate that CTs in conjunction with basal slip are likely the primary deformation modes under *c*-axis compression at room temperature. Pyramidal slip is, however, better suited to accommodate the deformation, and – with increasing temperature – this mode accounts for the majority of deformation. The full model captures this transition and the slip/twin activity more accurately than the reduced model and provides useful insight into the role of CTs in the given temperature range, highlighting the importance of this system.
- The representation and calibration of the CT systems is challenging, which imposes limitations onto the current model. The role of the CT system at lower temperature is likely *under*-approximated in the model—as in Zhang and Joshi (2012), Liu et al. (2017), who also predicted relatively strong activity of the pyramidal systems.
- The temperature dependence of the stress–strain response of Mg (and other Mg-alloys) results primarily from the activation of non-basal slip at higher temperature. The room temperature response of Mg (and Mg alloys) should, however, account for the important role of CTs.
- The Taylor assumption yields efficient and accurate polycrystal stress–strain predictions and qualitatively reasonable texture predictions, whereas more advanced homogenization approaches are required to spatially resolve microstructural details within and across grains. Investigations of the microstructure evolution of polycrystals with such techniques may overcome the limitations of the present model.

CRediT authorship contribution statement

Yannick Hollenweger: Methodology, Software, Validation, Investigation, Data curation, Visualization, Writing – original draft, Writing – review & editing. **Dennis M. Kochmann:** Conceptualization, Methodology, Writing – review & editing, Supervision, Funding acquisition.

Declaration of competing interest

The authors declare that they have no known competing financial interests or personal relationships that could have appeared to influence the work reported in this paper.

Data availability

Data will be made available on request.

Acknowledgments

References

Agnew, S.R., Duygulu, Ö., 2005. Plastic anisotropy and the role of non-basal slip in magnesium alloy AZ31B. Int. J. Plast. 21 (6), 1161–1193.

Agnew, S., Yoo, M., Tome, C., 2001. Application of texture simulation to understanding mechanical behavior of Mg and solid solution alloys containing Li or Y. Acta Mater. 49 (20), 4277–4289.

Akhtar, A., Teghtsoonian, E., 1969. Solid solution strengthening of magnesium single crystals-ii the effect of solute on the ease of prismatic slip. Acta Metall. 17 (11), 1351–1356. http://dx.doi.org/10.1016/0001-6160(69)90152-7.

Al-Samman, T., Li, X., Chowdhury, S.G., 2010. Orientation dependent slip and twinning during compression and tension of strongly textured magnesium AZ31 alloy. Mater. Sci. Eng. A 527 (15), 3450–3463.

Ando, S., Harada, N., Tsushida, M., Kitahara, H., Tonda, H., 2007. Temperature dependence of deformation behavior in magnesium and magnesium alloy single crystals. In: Key Engineering Materials. Vol. 345, Trans Tech Publ, pp. 101–104.

Ardeljan, M., Beyerlein, I.J., McWilliams, B.A., Knezevic, M., 2016. Strain rate and temperature sensitive multi-level crystal plasticity model for large plastic deformation behavior: Application to AZ31 magnesium alloy. Int. J. Plast. 83, 90–109. http://dx.doi.org/10.1016/j.ijplas.2016.04.005.

Asaro, R.J., Rice, J., 1977. Strain localization in ductile single crystals. J. Mech. Phys. Solids 25 (5), 309–338.

Barnett, M., 2007. Twinning and the ductility of magnesium alloys: Part ii.''contraction'' twins. Mater. Sci. Eng. A 464 (1–2), 8–16.

Barnett, M.R., Keshavarz, Z., Beer, A.G., Ma, X., 2008. Non-Schmid behaviour during secondary twinning in a polycrystalline magnesium alloy. Acta Mater. 56 (1), 5–15. http://dx.doi.org/10.1016/j.actamat.2007.08.034.

Basinski, Z., Szczerba, M., Niewczas, M., Embury, J., Basinski, S., 1997. The transformation of slip dislocations during twinning of copper-aluminum alloy crystals. Revue de Metallurgie 94 (9), 1037–1044.

Beausir, B., Biswas, S., Kim, D.I., Tóth, L.S., Suwas, S., 2009. Analysis of microstructure and texture evolution in pure magnesium during symmetric and asymmetric rolling. Acta Mater. 57 (17), 5061–5077.

Beyerlein, I.J., Tomé, C.N., 2004. Analytical modeling of material flow in equal channel angular extrusion (ECAE). Mater. Sci. Eng. A 380 (1), 171–190. http://dx.doi.org/10.1016/j.msea.2004.03.063.

Burke, E., Hibbard, W., 1952. Plastic deformation of magnesium single crystals. Jom 4 (3), 295–303.

Chakkedath, A., Maiti, T., Bohlen, J., Yi, S., Letzig, D., Eisenlohr, P., Boehlert, C., 2018. Contraction twinning dominated tensile deformation and subsequent fracture in extruded Mg-1Mn (Wt Pct) at ambient temperature. Metall. Mater. Trans. A 49 (6), 2441–2454.

Chang, Y., 2016. A Continuum Model for Slip-Twinning Interactions in Magnesium and Magnesium Alloys (Ph.D. thesis). California Institute of Technology, http://dx.doi.org/10.7907/Z96M34RX, URL https://resolver.caltech.edu/CaltechTHESIS:01252016-164549986.

Chang, Y., Kochmann, D.M., 2015. A variational constitutive model for slip-twinning interactions in hcp metals: Application to single- and polycrystalline magnesium. Int. J. Plast. 73, 39–61. http://dx.doi.org/10.1016/j.ijplas.2015.03.008.

Chang, Y., Lloyd, J.T., Becker, R., Kochmann, D.M., 2017. Modeling microstructure evolution in magnesium: Comparison of detailed and reduced-order kinematic models. Mech. Mater. 108, 40–57. http://dx.doi.org/10.1016/j.mechmat.2017.02.007.

Chapuis, A., Driver, J.H., 2011. Temperature dependency of slip and twinning in plane strain compressed magnesium single crystals. Acta Mater. 59 (5), 1986–1994. http://dx.doi.org/10.1016/j.actamat.2010.11.064.

Chen, Q., Hu, L., Shi, L., Zhou, T., Yang, M., Tu, J., 2020. Assessment in predictability of visco-plastic self-consistent model with a minimum parameter approach: Numerical investigation of plastic deformation behavior of AZ31 magnesium alloy for various loading conditions. Mater. Sci. Eng. A 774, 138912.

Christian, J.W., Mahajan, S., 1995. Deformation twinning. Prog. Mater. Sci. 39 (1–2), 1–157.

Clayton, J.D., Knap, J., 2011. A phase field model of deformation twinning: nonlinear theory and numerical simulations. Physica D 240 (9–10), 841–858.

Eswarappa Prameela, S., Yi, P., Hollenweger, Y., Liu, B., Chen, J., Kecskes, L., Kochmann, D.M., Falk, M., Weihs, T.P., 2021. Strengthening magnesium by design: integrating alloying and dynamic processing. arXiv e-prints arXiv–2105.

Homayonifar, M., Mosler, J., 2011. On the coupling of plastic slip and deformation-induced twinning in magnesium: A variationally consistent approach based on energy minimization. Int. J. Plast. 27 (7), 983–1003. http://dx.doi.org/10.1016/j.ijplas.2010.10.009.

Hu, Y., Turlo, V., Beyerlein, I.J., Mahajan, S., Lavernia, E.J., Schoenung, J.M., Rupert, T.J., 2020. Disconnection-mediated twin embryo growth in Mg. Acta Mater. 194, 437–451.

Huang, K., Logé, R.E., 2016. A review of dynamic recrystallization phenomena in metallic materials. pp. 548–574. http://dx.doi.org/10.1016/j.matdes.2016.09.012.

Jain, A., Agnew, S., 2007. Modeling the temperature dependent effect of twinning on the behavior of magnesium alloy AZ31B sheet. Mater. Sci. Eng. A 462 (1–2), 29–36.

Jones, E., Oliphant, T., Peterson, P., et al., 2001. Scipy: Open source scientific tools for Python. URL http://www.scipy.org/.

Kaibyshev, R., 2012. Dynamic recrystallization in magnesium alloys. In: Advances in Wrought Magnesium Alloys. Elsevier, pp. 186–225.

Kalidindi, S.R., 1998. Incorporation of deformation twinning in models. Int. J. Plast. 46 (2), 267–290.

Kang, F., Li, Z., Wang, J.T., Cheng, P., Wu, H.Y., 2012. The activation of< c+ a> non-basal slip in magnesium alloys. J. Mater. Sci. 47 (22), 7854–7859.

Kecskes, L.J., Krywopusk, N.M., Hollenweger, Y., Krynicki, J.N., Prameela, S.E., Yi, P., Liu, B., Falk, M.L., Kochmann, D.M., Weihs, T.P., 2021. Recrystallization mechanisms, grain refinement, and texture evolution during ECAE processing of Mg and its alloys. Mech. Mater. 162, 104067.

Kelley, E., Hosford, W., 1967. Kelley_and_Hosford.pdf (Ph.D. thesis). University of Michigan.

Khosravani, A., Scott, J., Miles, M., Fullwood, D., Adams, B., Mishra, R., 2013. Twinning in magnesium alloy AZ31B under different strain paths at moderately elevated temperatures. Int. J. Plast. 45, 160–173.

Kitahara, T., Ando, S., Tsushida, M., Kitahara, H., Tonda, H., 2007. Deformation behavior of magnesium single crystals in c-axis compression. In: Key Engineering Materials. Vol. 345, Trans Tech Publ, pp. 129–132.

Knezevic, M., Al-Harbi, H.F., Kalidindi, S.R., 2009. Crystal plasticity simulations using discrete Fourier transforms. Acta Mater. 57 (6), 1777–1784.

Knezevic, M., Levinson, A., Harris, R., Mishra, R.K., Doherty, R.D., Kalidindi, S.R., 2010. Deformation twinning in AZ31: influence on strain hardening and texture evolution. Acta Mater. 58 (19), 6230–6242.

Koike, J., Kobayashi, T., Mukai, T., Watanabe, H., Suzuki, M., Maruyama, K., Higashi, K., 2003. The activity of non-basal slip systems and dynamic recovery at room temperature in fine-grained AZ31B magnesium alloys. Acta Mater. 51 (7), 2055–2065.

Kulekci, M.K., 2008. Magnesium and its alloys applications in automotive industry. Int. J. Adv. Manuf. Technol. 39 (9–10), 851–865.

Kweon, S., Raja, D.S., 2021. A study on the mechanical response of magnesium using an anisotropic elasticity twinning CP FEM. Arch. Appl. Mech. 1–23.

Lee, S., Chen, Y.H., Wang, J.Y., 2002. Isothermal sheet formability of magnesium alloy AZ31 and AZ61. J. Mater Process. Technol. 124 (1–2), 19–24. http://dx.doi.org/10.1016/S0924-0136(02)00038-9.

Lilleodden, E., 2010. Microcompression study of Mg (0 0 0 1) single crystal. Scr. Mater. 62 (8), 532–535.

Liu, Q., Roy, A., Silberschmidt, V.V., 2017. Temperature-dependent crystal-plasticity model for magnesium: A bottom-up approach. Mech. Mater. 113, 44–56. http://dx.doi.org/10.1016/j.mechmat.2017.07.008.

Liu, C., Shanthraj, P., Robson, J.D., Diehl, M., Dong, S., Dong, J., Ding, W., Raabe, D., 2019a. On the interaction of precipitates and tensile twins in magnesium alloys. Acta Mater. 178, 146–162. http://dx.doi.org/10.1016/j.actamat.2019.07.046, arXiv:1906.08736.

Liu, C., Shanthraj, P., Robson, J.D., Diehl, M., Dong, S., Dong, J., Ding, W., Raabe, D., 2019b. On the interaction of precipitates and tensile twins in magnesium alloys. Acta Mater. 178, 146–162. http://dx.doi.org/10.1016/j.actamat.2019.07.046, arXiv:1906.08736.

Mirzadeh, H., 2014. Constitutive analysis of Mg–Al–Zn magnesium alloys during hot deformation. Mech. Mater. 77, 80–85.

Mordike, B., Ebert, T., 2001. Magnesium: properties—applications—potential. Mater. Sci. Eng. A 302 (1), 37–45.

Muránsky, O., Carr, D., Barnett, M., Oliver, E., Šittner, P., 2008. Investigation of deformation mechanisms involved in the plasticity of AZ31 Mg alloy: In situ neutron diffraction and EPSC modelling. Mater. Sci. Eng. A 496 (1–2), 14–24.

Nie, J.F., Shin, K.S., Zeng, Z.R., 2020. Microstructure, deformation, and property of wrought magnesium alloys. In: Metallurgical and Materials Transactions a: Physical Metallurgy and Materials Science. Vol. 51, (12), Springer US, pp. 6045–6109. http://dx.doi.org/10.1007/s11661-020-05974-z.

Obara, T., Yoshinga, H., Morozumi, S., 1973. {1122}<1123> Slip system in magnesium. Acta Metall. 21 (7), 845–853.

Ono, N., Nowak, R., Miura, S., 2004. Effect of deformation temperature on Hall-Petch relationship registered for polycrystalline magnesium. Mater. Lett. 58 (1–2), 39–43. http://dx.doi.org/10.1016/S0167-577X(03)00410-5.

Proust, G., Tomé, C., Kaschner, G., 2007. Modeling texture, twinning and hardening evolution during deformation of hexagonal materials. Acta Mater. 55 (6), 2137–2148.

Reed-Hill, R.E., Robertson, W.D., 1957. The crystallographic characteristics of fracture in magnesium single crystals. Acta Metall. 5 (12), 728–737. http://dx.doi.org/10.1016/0001-6160(57)90075-5.

Roy, A., Nani, E.S., Lahiri, A., Gururajan, M.P., 2017. Interfacial free energy anisotropy driven faceting of precipitates. Phil. Mag. 97 (30), 2705–2735. http://dx.doi.org/10.1080/14786435.2017.1348633.

Sahoo, S.K., Biswas, S., Toth, L.S., Gautam, P., Beausir, B., 2020. Strain hardening, twinning and texture evolution in magnesium alloy using the all twin variant polycrystal modelling approach. Int. J. Plast. 128, 102660.

Sandlöbes, S., Zaefferer, S., Schestakow, I., Yi, S., Gonzalez-Martinez, R., 2011. On the role of non-basal deformation mechanisms for the ductility of Mg and Mg–Y alloys. Acta Mater. 59 (2), 429–439.

Sebastian, W., Dröder, K., Schumann, S., 2000. Properties and processing of magnesium wrought products for automotive applications. Magnes. Alloys Appl. 602–608.

Sitdikov, O., Kaibyshev, R., 2001. Dynamic recrystallization in pure magnesium. Mater. Trans. 42 (9), 1928–1937.

Staroselsky, A., Anand, L., 2003. A constitutive model for hcp materials deforming by slip and twinning: application to magnesium alloy AZ31B. Int. J. Plast. 19 (10), 1843–1864.

Styczynski, A., Hartig, C., Bohlen, J., Letzig, D., 2004. Cold rolling textures in AZ31 wrought magnesium alloy. Scr. Mater. 50 (7), 943–947.

Takuda, H., Fujimoto, H., Hatta, N., 1998. Modelling on flow stress of Mg-Al-Zn alloys at elevated temperatures. J. Mater Process. Technol. 80–81, 513–516. http://dx.doi.org/10.1016/S0924-0136(98)00154-X.

Tam, K.J., Vaughan, M.W., Shen, L., Knezevic, M., Karaman, I., Proust, G., 2020. Modelling the temperature and texture effects on the deformation mechanisms of magnesium alloy AZ31. Int. J. Mech. Sci. 182 (May), http://dx.doi.org/10.1016/j.ijmecsci.2020.105727.

Tomé, C.N., Lebensohn, R.A., Kocks, U.F., 1991. A model for texture development dominated by deformation twinning: Application to zirconium alloys. Acta Metall. Mater. 39 (11), 2667–2680. http://dx.doi.org/10.1016/0956-7151(91)90083-D.

Tutcuoglu, A.D., Hollenweger, Y., Stoy, A., Kochmann, D.M., 2019a. High- vs. low-fidelity models for dynamic recrystallization in copper. Materialia 7 (July), 100411. http://dx.doi.org/10.1016/j.mtla.2019.100411.

Tutcuoglu, A.D., Vidyasagar, A., Bhattacharya, K., Kochmann, D.M., 2019b. Stochastic modeling of discontinuous dynamic recrystallization at finite strains in hcp metals. J. Mech. Phys. Solids 122, 590–612. http://dx.doi.org/10.1016/j.jmps.2018.09.032.

Vidyasagar, A., Tutcuoglu, A.D., Kochmann, D.M., 2018. Deformation patterning in finite-strain crystal plasticity by spectral homogenization with application to magnesium. Comput. Methods Appl. Mech. Engrg. 335, 584–609. http://dx.doi.org/10.1016/j.cma.2018.03.003.

Walde, T., Riedel, H., 2007. Modeling texture evolution during hot rolling of magnesium alloy AZ31. Mater. Sci. Eng. A 443 (1–2), 277–284. http://dx.doi.org/10.1016/j.msea.2006.09.028.

Wang, X., Hu, Y., Yu, K., Mahajan, S., Beyerlein, I.J., Lavernia, E.J., Rupert, T.J., Schoenung, J.M., 2022. Room temperature deformation-induced solute segregation and its impact on twin boundary mobility in a Mg-Y alloy. Scr. Mater. 209, 114375.

Wang, W., Liu, J., Soh, A.K., 2019. Crystal plasticity modeling of strain rate and temperature sensitivities in magnesium. Acta Mech. 230 (6), 2071–2086. http://dx.doi.org/10.1007/s00707-019-2374-9.

Wei, G., Peng, X., Hadadzadeh, A., Mahmoodkhani, Y., Xie, W., Yang, Y., Wells, M.A., 2015. Constitutive modeling of Mg–9Li–3Al–2Sr–2Y at elevated temperatures. Mech. Mater. 89, 241–253.

Wonsiewicz, B.C., Backofen, W.A., 1967. Plasticity of magnesium single crystals. Trans. Metall. Soc. AIME 239, 1422–1431.

Xie, K.Y., Alam, Z., Caffee, A., Hemker, K.J., 2016. Pyramidal I slip in c-axis compressed Mg single crystals. Scr. Mater. 112, 75–78.

Xin, Y., Wang, M., Zeng, Z., Huang, G., Liu, Q., 2011. Tailoring the texture of magnesium alloy by twinning deformation to improve the rolling capability. Scr. Mater. 64 (10), 986–989.

Yi, P., Cammarata, R.C., Falk, M.L., 2017. Solute softening and defect generation during prismatic slip in magnesium alloys. Modelling Simulation Mater. Sci. Eng. 25 (8), 1–16. http://dx.doi.org/10.1088/1361-651X/aa87fc.

Yi, P., Sasaki, T., Prameela, S.E., Weihs, T.P., Falk, M.L., 2021. The interplay between solute atoms and vacancy clusters in magnesium alloys. arXiv preprint arXiv:2112.03894.

Yoo, M.H., 1981. Slip, twinning, and fracture in hexagonal close-packed metals. Metall. Trans. A 12 (3), 409–418. http://dx.doi.org/10.1007/BF02648537.

Yoo, M., Wei, C., 1967. Slip modes of hexagonal-close-packed metals. J. Appl. Phys. 38 (11), 4317–4322.

Yoshinaga, H., Horiuchi, R., 1963. Trans. JIM. Trans. JIM 4, 134–141.

Yoshinaga, H., Horiuchi, R., 1964. On the nonbasal slip in magnesium crystals. Trans. Japan Inst. Met. 5 (1), 14–21.

Yoshinaga, H., Obara, T., Morozumi, S., 1973. Twinning deformation in magnesium compressed along the C-axis. Mater. Sci. Eng. 12 (5–6), 255–264.

Yu, H., Xin, Y., Wang, M., Liu, Q., 2018. Hall-petch relationship in Mg alloys: A review. J. Mater. Sci. Technol. 34 (2), 248–256. http://dx.doi.org/10.1016/j.jmst.2017.07.022.

Zecevic, M., Beyerlein, I.J., Knezevic, M., 2018. Activity of pyramidal I and II< c+ a> slip in Mg alloys as revealed by texture development. J. Mech. Phys. Solids 111, 290–307.

Zeng, Z., Nie, J.-F., Xu, S.-W., HJ Davies, C., Birbilis, N., 2017. Super-formable pure magnesium at room temperature. Nature Commun. 8 (1), 1–6.

Zhang, J., Joshi, S.P., 2012. Phenomenological crystal plasticity modeling and detailed micromechanical investigations of pure magnesium. J. Mech. Phys. Solids 60 (5), 945–972. http://dx.doi.org/10.1016/j.jmps.2012.01.005.

Zhou, B., 2016. Lean principles, practices, and impacts: a study on small and medium-sized enterprises (SMEs). Ann. Oper. Res. 241 (1–2), 457–474. http://dx.doi.org/10.1007/s10479-012-1177-3.

Zhou, B., Sui, M., 2019. High density stacking faults of 101−1 compression twin in magnesium alloys. J. Mater. Sci. Technol. 35 (10), 2263–2268.